processes

MDPI

Article

Radial Basis Function Based Meta-Heuristic Algorithms for Parameter Extraction of Photovoltaic Cell

Peng He [1], Xinze Xi [1], Shengnan Li [1], Wenlong Qin [1], Chao Xing [1] and Bo Yang [2,*]

[1] Electric Power Science Institute, Yunnan Power Grid Co., Ltd., Kunming 650000, China; hepeng08@yn.csg.cn (P.H.); cs_xxz@163.com (X.X.); lishengnan@dlyjy.yn.csg.cn (S.L.); qwl11@outlook.com (W.Q.); xingchao22@outlook.com (C.X.)

[2] Faculty of Electric Power Engineering, Kunming University of Science and Technology, Kunming 650500, China

* Correspondence: yangbo_ac@outlook.com

Abstract: Accurate parameter estimation of photovoltaic (PV) cells is crucial for establishing a reliable cell model. Based on this, a series of studies on PV cells can be conducted more effectively to improve power output; an accurate model is also crucial for the operation and control of PV systems. However, due to the high nonlinearity of the cell and insufficient measured current and voltage data, traditional PV parameter identification methods are difficult to solve this problem. This article proposes a parameter identification method for PV cell models based on the radial basis function (RBF). Firstly, RBF is used to de-noise and predict the data to solve the current problems in the parameter identification field of noise data and insufficient data. Then, eight prominent meta-heuristic algorithms (MhAs) are used to identify the single-diode model (SDM), double-diode model (DDM), and three-diode model (TDM) parameters of PV cells. By comparing the identification accuracy of the three models in two datasets in detail, the final results show that this method can effectively achieve parameter extraction, with advantages such as high extraction accuracy and stability, greatly improving the accuracy and reliability of parameter identification. Especially in the TDM, the *I-V* data and *P-V* data obtained from the PV model established through the identified parameters have very high fitting accuracy with the measured *I-V* and *P-V* data, reaching 99.58% and 99.65%, respectively. The research can effectively solve the low accuracy problem caused by insufficient data and noise data in the traditional method of identifying PV cells and can greatly improve the accuracy of PV cell modeling. It is of great significance for the operation and control of PV systems.

Keywords: parameter identification/extraction; PV cell; RBF; meta-heuristic algorithm; artificial neural network; PV cell model

Citation: He, P.; Xi, X.; Li, S.; Qin, W.; Xing, C.; Yang, B. Radial Basis Function Based Meta-Heuristic Algorithms for Parameter Extraction of Photovoltaic Cell. *Processes* **2023**, *11*, 1606. https://doi.org/10.3390/pr11061606

Academic Editor: Olympia Roeva

Received: 18 April 2023
Revised: 8 May 2023
Accepted: 18 May 2023
Published: 24 May 2023

1. Introduction

Since entering the industrialized society, human science and technology have made breakthrough development and maintained a very fast development speed. At the same time, the massive development and large-scale use of fossil energy are the basic conditions for maintaining the normal operation of industrial society. With the continuous growth of the population and the rapid development of society, human demand for traditional fossil energy is increasing. However, contrary to this, fossil energy is non-renewable and not inexhaustible. Overexploitation and use of various fossil energy will lead to the global energy crisis [1]. Moreover, due to the extensive use of fossil fuels can also cause huge pollution, leading to environmental problems such as the greenhouse effect and ecological destruction [2]. With a series of energy crises and environmental pollution problems emerging one after another, it is urgent to change the energy consumption structure, vigorously develop renewable energy, and take the road of sustainable development to protect the environment, and countries around the world have reached a consensus [3].

As is well known, solar energy is the most easily obtainable renewable energy in daily life, with the characteristic of being inexhaustible, safe, reliable, and easily obtainable. Therefore, the development and utilization of solar energy have great significance for global development [4]. Among them, significant breakthroughs have been made in the research of photovoltaic (PV) power generation technology. PV power generation technology mainly utilizes the PV effect to directly convert solar energy into electrical energy through PV cells. PV cell is the core components of PV power generation systems, and the efficiency of PV power generation is not only related to the temperature and light intensity in the external environment [5] but also closely related to the parameters of the internal structure of PV cells. Therefore, precise modeling of PV cells and studying their internal model parameters are of great significance for improving the power generation efficiency of PV systems [6–8]. At present, there are three most common models for PV cells, namely the single-diode model (SDM) [9,10], the double-diode model (DDM), and the three-diode model (TDM) [11], each with its unique features. Among them, SDM has the characteristics of a simple control structure and low implementation cost, while DDM has the characteristics of simple hardware implementation and low circuit complexity. TDM has the highest complexity, but the curve fitting accuracy is also the most accurate. Among them, precise identification of some cell parameters in the above-mentioned PV cell model is not only conducive to achieving accurate PV cell modeling but also has significant significance for studying the output characteristic of PV cells and improving the power generation efficiency of PV systems. At present, there have been many studies on the identification of PV cell parameters. Due to the high nonlinearity and multimodality of PV cells, it is difficult to obtain the optimal solution using traditional optimization methods. Moreover, due to the special structure of PV cells, the amount of measured current-voltage data is also very small, which greatly increases the difficulty of PV cell parameter identification [12]. In addition, the insufficient amount of measured data and noise data also make the traditional PV cell parameter identification accuracy low, which poses a serious challenge to the operation and control of PV systems and the improvement of the output power of the system. The proposed heuristic algorithm and radial basis function (RBF) can effectively solve the above problems. It has the ability to search globally, can avoid falling into the optimal situation, and can accurately identify the parameters of the nonlinear system. Reference [13] proposed an improved cuckoo search algorithm for parameter identification of PV cell modules, constructed an improved cuckoo search based on the cross-entropy method, and realized accurate PV cell parameter identification using the cross entropy global optimization and cuckoo search synergy. The final results show that this method can accurately identify PV cell parameters and also has fast convergence speed, high optimization accuracy, and good global optimization performance. Reference [14] proposed a parameter identification method for SDM and DDM based on the whale optimization algorithm. The parameters identified by the whale optimization algorithm were compared and verified with the results obtained from the simulation of PV modules, ultimately fully proving that the whale optimization algorithm (WOA) can be effectively applied to the parameter identification of PV cells. In reference [15], a PV cell parameter identification method based on an improved adaptive particle swarm optimization algorithm was proposed, which can effectively solve the problems of local optimization and low identification accuracy when traditional particle swarm optimization identifies PV cell parameters. The average relative error of the final results is below 3%, fully proving its feasibility and effectiveness. Reference [16] proposed a PV module parameter identification method based on the grey wolf optimization algorithm (GWO), fully considering the impact of weather conditions on cell parameter extraction. Finally, the identification results were compared with those obtained by particle swarm optimization (PSO). Reference [17] proposed a PV cell parameter identification method based on the imperialist competition algorithm (ICA), using ICA to study the SDM and DDM of PV cells and considering the effects of radiation and temperature on PV cells. The final results can prove its effectiveness and reliability in PV cell parameter identification. Reference [18] proposed a JAYA algorithm for PV cell parameter identification, which

quantifies the individual performance in the population using probability and then selects the evolutionary strategy of each individual based on probability. Through the above mechanism, the algorithm's search and optimization capabilities are improved. Three typical diode models were identified for parameters in the article, and the final results fully demonstrate that the performance-guided JAYA (PGJAYA) algorithm has good robustness and high accuracy in parameter identification. Reference [19] proposed a parameter identification of TDM of PV module based on the coyote optimization algorithm (COA), fully considered the impact of temperature and radiant intensity on PV cell, and then conducted parameter identification of TDM of two PV models, fully verifying the effectiveness of this method in the field of parameter identification. Reference [20] proposed an improved equalizer optimization algorithm for PV cell parameter identification. The improved balance optimizer uses a backpropagation neural network to predict the output data of PV cells, which can achieve more efficient optimization and effectively improve the accuracy and reliability of PV cell parameter identification optimization. Reference [12] proposed a PV cell parameter identification method based on a data prediction heuristic algorithm. In this paper, the limit learning machine is used to train and predict the measured data, providing an accurate and reliable fitness function for the heuristic algorithm and enhancing its global exploration and local search capabilities. The final results also show that the accuracy of identification can be greatly improved, and the convergence speed can be accelerated. In reference [21], a two-stage PV parameter cell identification method based on maximum power matching and an improved airflow direction algorithm was proposed. Maximum power matching (MPM) was used for coarse extraction, and the improved flow direction algorithm (IFDA) was used for precise identification. The effects of various algorithms were compared, and multiple repeated experiments were conducted. The final results also proved that this method has good identification accuracy and robustness.

At present, research on PV cell identification mainly uses heuristic algorithms for parameter identification, but there is less processing and research on measured data. This paper proposes meta-heuristic algorithms (MhAs) for PV cell parameter identification based on RBF, which de-noises, trains, and predicts through RBF data [22] and then uses MhAs for parameter identification processing [23]. The final results also fully demonstrate that the extraction accuracy after data de-noising and prediction is higher than that of the original data. This article opens up a new direction for the identification of PV cell parameters, starting from fitting data and studying the impact of measured *I-V* data on the identification effect, providing new ideas for the research of PV cell parameter identification. The contributions and innovations of this article can be summarized as follows.

1. Three types of PV models were established, and parameter identification was performed on all three models;
2. Considering the impact of noise data on recognition accuracy, using RBF to de-noise and identify the parameters of the three diode models under two conditions, original data and de-noise data, respectively;
3. Considering the impact of insufficient measured *I-V* data on recognition accuracy, using RBF to de-noise and identify the parameters of the three diode models under two conditions, original data, and predicted data, respectively;
4. Based on the results of RBF data processing, the effectiveness of eight typical heuristic algorithms in PV cell parameter identification is compared, and it was ultimately proven that *I-V* data after data processing could greatly improve extraction accuracy when used for parameter identification.

The remaining content of this article is as follows: Section 2 is the PV cell modeling section, which mainly introduces three typical PV cell models and establishes objective functions for parameter identification of each model; Section 3 introduces how RBF-MhAs is applied to PV parameter extraction research, and then introduces RBF application for data de-noising and data prediction; In Section 4, the parameter results obtained from the final identification of three cell models are mainly presented; Section 5 is the discussion section; Section 6 is a summary section, providing important conclusions and prospects.

2. PV Modeling

Establishing a PV cell model is beneficial for deeper research on parameter identification and output characteristic of PV cells. At present, there are three common models of PV cells, namely SDM, DDM, and TDM [2].

2.1. Mathematical Modeling

2.1.1. SDM

SDM is composed of an ideal constant current source I_{ph}, diode D, series resistor R_s, and parallel resistor R_{sh}, as shown in Figure 1 [11].

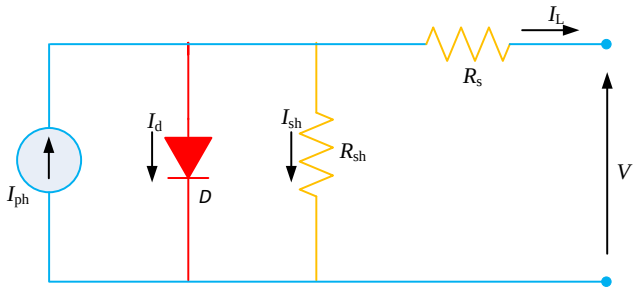

Figure 1. SDM of PV cell.

The relationship between the output current I and the output voltage V of the PV cell SDM is as follows.

$$I_L = I_{ph} - I_d\left[\exp\left(\frac{V_L + I_L R_s}{aV_T}\right) - 1\right] - \frac{V_L + I_L R_s}{R_{sh}} \tag{1}$$

$$V_T = \frac{KT}{q} \tag{2}$$

where V_T represents thermal voltage, I_{ph} is an ideal constant current source, q is the amount of electronic charge, and the value is $q = 1.6 \times 10^{-19}$ C, $K = 1.38 \times 10^{-23}$ J/K represents Boltzmann constant, T represents cell temperature, I_L and V_L represents the cell output current and output voltage, respectively. R_{sh} represents shunt resistance, I_d is the reverse saturation current of the diode, a is the diode quality factor, and R_s is the series resistance, respectively.

From the above equation, it can be seen that there are a total of 5 unknown parameters in SDM that need to be identified, namely I_{ph}, I_d, R_s, R_{sh}, and a.

2.1.2. DDM

Compared to SDM, DDM has an additional diode in parallel, which has better accuracy in performance, but the model is also relatively more complex. The schematic diagram is shown in Figure 2 [24].

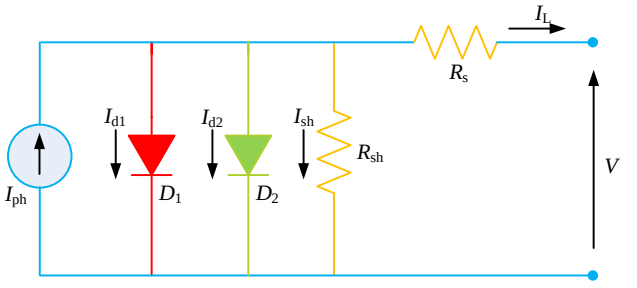

Figure 2. DDM of PV cell.

The relationship between I and V in DDM is shown in the following equation.

$$I_L = I_{ph} - I_{d1}\left[\exp\left(\frac{q(V_L + I_L R_s)}{a_1 V_T}\right) - 1\right] - I_{d2}\left[\exp\left(\frac{q(V_L + I_L R_s)}{a_2 V_T}\right) - 1\right] - \frac{V_L + I_L R_s}{R_{sh}} \quad (3)$$

where I_{d1} is the reverse saturation current of diode D_1, I_{d2} is the reverse saturation current of diode D_2, a_1 is the quality factor of diode D_1, and a_2 is the quality factor of diode D_2, respectively.

Therefore, the parameters that DDM needs to recognize are I_{ph}, I_{d1}, R_s, R_{sh}, a_1, I_{d2} and a_2.

2.1.3. TDM

The schematic diagram of TDM is shown in Figure 3, which has the highest complexity but also the highest accuracy among the three models.

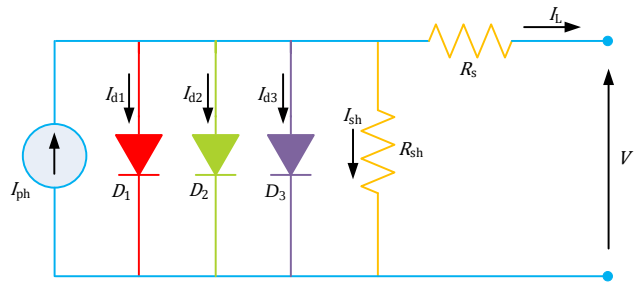

Figure 3. TDM of PV cell.

The relationship between I and V in TDM is as follows.

$$\begin{aligned} I_L = I_{ph} - I_{d1}\left[\exp\left(\frac{q(V_L+I_L R_s)}{a_1 V_T}\right) - 1\right] - I_{d2}\left[\exp\left(\frac{q(V_L+I_L R_s)}{a_2 V_T}\right) - 1\right] \\ - I_{d3}\left[\exp\left(\frac{q(V_L+I_L R_s)}{a_3 V_T}\right) - 1\right] - \frac{V_L+I_L R_s}{R_{sh}} \end{aligned} \quad (4)$$

where I_{d1} is the reverse saturation current of diode D_1, I_{d2} is the reverse saturation current of diode D_2, I_{d3} is the reverse saturation current of diode D_3, a_1 is the quality factor of diode D_1, a_2 is the quality factor of diode D_2, and a_3 is the quality factor of diode D_3, respectively.

Therefore, the parameters that TDM needs to recognize are I_{ph}, I_{d1}, R_s, R_{sh}, a_1, I_{d2}, a_2, I_{d3}, and a_3.

2.2. Objective Function

When quantitatively and effectively evaluating the effectiveness of PV cell parameter identification, appropriate evaluation indicators are needed to evaluate the quality of the results through evaluation criteria. This article selects root mean square error (RMSE) as the objective function, and its calculation method is as follows.

$$\mathrm{RMSE}(x) = \sqrt{\frac{1}{N}\sum_{k=1}^{N}(f(V_L, I_L, x))^2} \quad (5)$$

where x is the solution vector of the unknown parameter to be identified, and N is the number of experimental data points.

In the article, parameter identification was conducted for three cell models, and the objective functions and solution vector of each model were summarized as follows [11].

$$f_{SDM}(V_L, I_L, x) = I_{ph} - I_d\left[\exp\left(\frac{V_L + I_L R_s}{a V_T}\right) - 1\right] - \frac{V_L + I_L R_s}{R_{sh}} - I_L \quad (6)$$

$$f_{DDM}(V_L, I_L, x) = I_{ph} - I_{d1}\left[\exp\left(\frac{q(V_L + I_L R_s)}{a_1 V_T}\right) - 1\right] - I_{d2}\left[\exp\left(\frac{q(V_L + I_L R_s)}{a_2 V_T}\right) - 1\right] - \frac{V_L + I_L R_s}{R_{sh}} - I_L \quad (7)$$

$$f_{\mathrm{TDM}}(V_{\mathrm{L}}, I_{\mathrm{L}}, x) = I_{\mathrm{ph}} - I_{\mathrm{d1}}\left[\exp\left(\frac{q(V_{\mathrm{L}}+I_{\mathrm{L}}R_{\mathrm{s}})}{a_1 V_{\mathrm{T}}}\right) - 1\right] - I_{\mathrm{d2}}\left[\exp\left(\frac{q(V_{\mathrm{L}}+I_{\mathrm{L}}R_{\mathrm{s}})}{a_2 V_{\mathrm{T}}}\right) - 1\right] - I_{\mathrm{d3}}\left[\exp\left(\frac{q(V_{\mathrm{L}}+I_{\mathrm{L}}R_{\mathrm{s}})}{a_3 V_{\mathrm{T}}}\right) - 1\right] - \frac{V_{\mathrm{L}}+I_{\mathrm{L}}R_{\mathrm{s}}}{R_{\mathrm{sh}}} - I_{\mathrm{L}} \tag{8}$$

$$x = \begin{cases} \left\{I_{\mathrm{ph}}, I_{\mathrm{sd}}, R_{\mathrm{s}}, R_{\mathrm{sh}}, a\right\}_{\mathrm{SDM}} \\ \left\{I_{\mathrm{ph}}, I_{\mathrm{d1}}, a_1, R_{\mathrm{s}}, R_{\mathrm{sh}}, I_{\mathrm{d2}}, a_2\right\}_{\mathrm{DDM}} \\ \left\{I_{\mathrm{ph}}, I_{\mathrm{d1}}, a_1, R_{\mathrm{s}}, R_{\mathrm{sh}}, I_{\mathrm{d2}}, a_2, I_{\mathrm{d3}}, a_3\right\}_{\mathrm{TDM}} \end{cases} \tag{9}$$

3. RBF-MhAs for PV Parameter Extraction

3.1. Principle of RBF

RBF neural network is a classic model of artificial neural networks belonging to feedforward neural networks. It has good generalization ability and fast convergence speed and can approximate any function with high accuracy. It is commonly used to fit nonlinear maps [25]. It utilizes strict interpolation methods in multidimensional space to provide a set of functions for hidden units, which construct an arbitrary basis for the input vector when it is extended to the hidden space. The functions in this set are the base functions. RBF is composed of an input layer, a hidden layer, and an output layer. The input layer is composed of signal source nodes, connecting the external environment and network. The transformation function of the hidden layer is the RBF, which is used as the nonlinear transformation from the input vector space to the hidden layers [26,27]. The output layer linearly combines the hidden layers to output certain vector target features. The schematic diagram of RBF is shown in Figure 4.

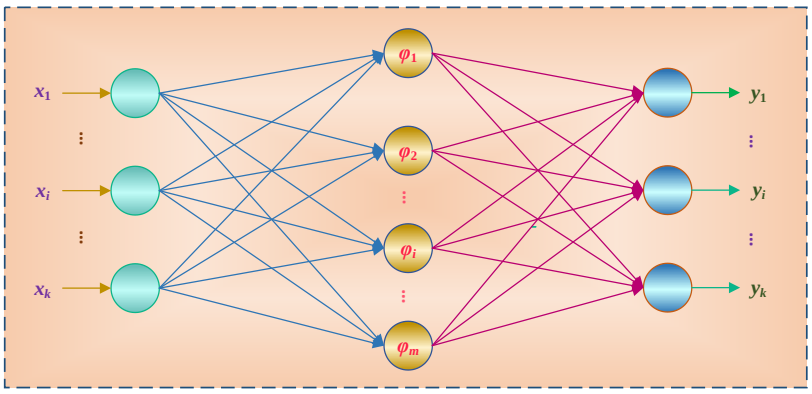

Figure 4. RBF neural network.

The expression of RBF is as follows [28].

$$f(x) \simeq f^*(x) = \sum_{k=1}^{m} \lambda_i \varphi(\|x - x_k\|) \tag{10}$$

where $f^*(x)$ is the approximation function, x is the input variable, m is the number of sample points, and x_k is the space vector of the kth sample point; $\boldsymbol{\lambda}^{m\times 1} = [\lambda_1, \lambda_2, \ldots \lambda_m]$ is the undetermined coefficient of RBF, $\|x - x_k\|$ is the Euclidean norm, φ is a base function.

The commonly used RBF is a linear function, cubic function, and Gaussian function, as shown in the following formula [29].

$$\varphi(\|x - x_k\|) = r * \|x - x_k\| \tag{11}$$

$$\varphi(\|x - x_k\|) = (r + \|x - x_k\|)^3 \tag{12}$$

$$\varphi(\|x - x_k\|) = \mathrm{e}^{-\|x-x_k\|^2 * r^2} \tag{13}$$

where r is the coefficient of RBF.

The undetermined coefficient of RBF λ is determined by the following equation.

$$\boldsymbol{\phi}^{m\times m}\boldsymbol{\lambda}^{m\times 1} = \boldsymbol{Y}^{m\times 1} \tag{14}$$

$$\boldsymbol{\phi}^{m\times m} = \begin{bmatrix} \varphi(\|x_1 - x_1\|) & \cdots & \varphi(\|x_1 - x_m\|) \\ \vdots & \ddots & \vdots \\ \varphi(\|x_m - x_1\|) & \cdots & \varphi(\|x_m - x_m\|) \end{bmatrix} \tag{15}$$

$$\boldsymbol{Y}^{m\times 1} = [f(x_1), f(x_2), \ldots, f(x_m)] \tag{16}$$

where m is the number of sample points.

The most special feature of RBF is it uses the basis of the hidden layer basis function to form a hidden layer space. In this way, the input vector can be mapped to the hidden space without weight, while the mapping from the hidden layer to the output space is linear; that is, the output of RBF is a linear weighted sum of unit outputs. Different from traditional data processing methods such as group method of data handling (GMDH), GMDH increases the complexity of the research due to the interrelationships between research data [30,31]. RBF has the advantages of simple structure, simple training, fast learning convergence, and can approximate any nonlinear function.

3.2. RBF for I-V Data Preprocessing

3.2.1. RBF for *I-V* Data De-Noising

As is well known, the measured *I-V* data of PV cells inevitably contain noise under various complex operating conditions and actual operating conditions. Due to the influence of noise, the application of MhAs for parameter identification can lead to inaccurate final identification results, seriously affecting the effectiveness of PV parameter identification and PV cell modeling.

Therefore, in order to eliminate the impact of noise on the results, this article adopts RBF to further link and reduce data noise by connecting the weights between the input layer and the hidden layer [32]. The results of de-noising through RBF are shown in Figure 5. It can be seen that the fitting accuracy of noise data and de-noise data is very high compared to the original data, with the fitting correlation coefficients R^2_{N} and R^2_{DN} of 98.69% and 99.98%, respectively.

3.2.2. RBF for *I-V* Data Prediction

Identifying PV cell parameters essentially involves fitting *I-V* data, and the final identification accuracy depends heavily on voltage and current data. However, it is difficult to obtain actual cell voltage and current data. Therefore, this article uses RBF to train existing *I-V* data and then perform data prediction to expand the data volume. The results of prediction through RBF are shown in Figure 6. It can also be seen that the data predicted by RBF also has extremely high fitting accuracy with the original data and the fitting correlation coefficient R^2_{P} is 99.98%.

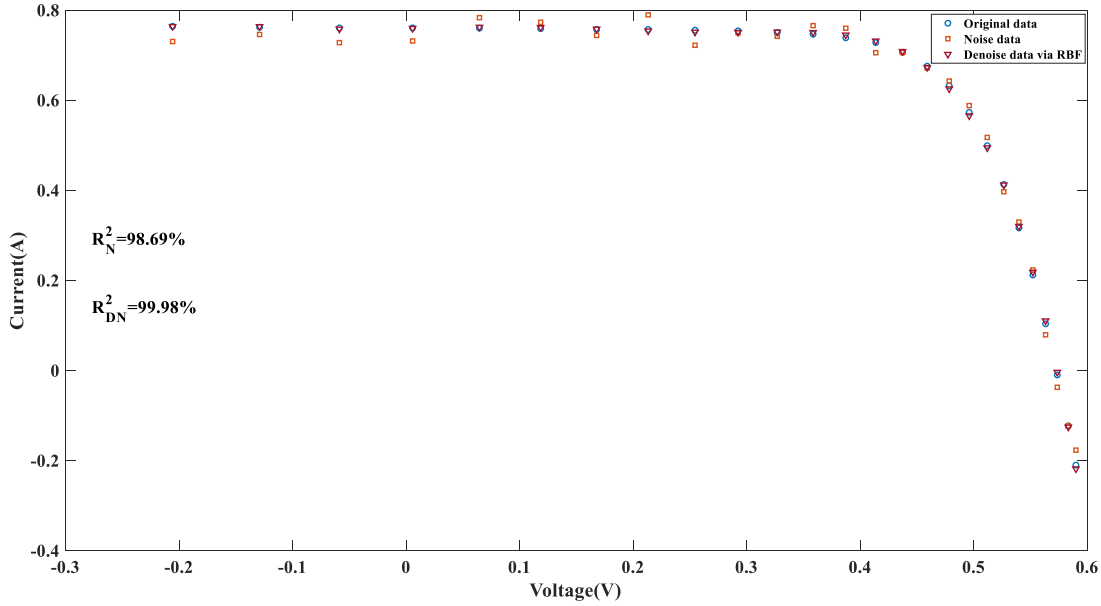

Figure 5. Result of RBF data de-noising.

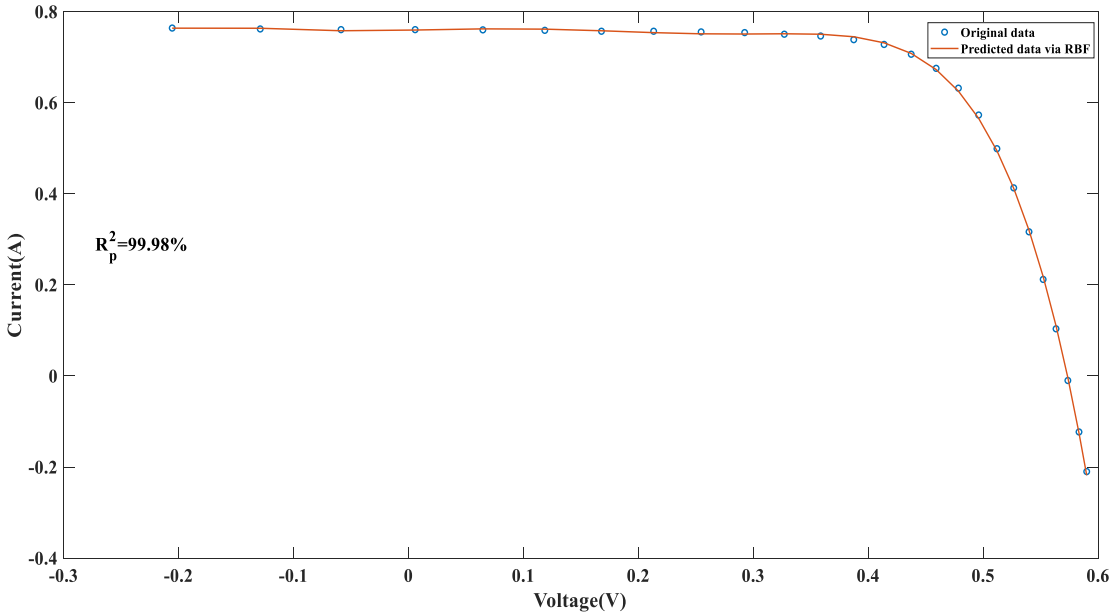

Figure 6. Result of RBF data prediction.

3.3. General Execution of Parameter Extraction

The general process of PV cell parameter identification based on RBF-MhAs in this article mainly includes three parts: data collection, data preprocessing, and optimal parameter extraction, as shown in Figure 7.

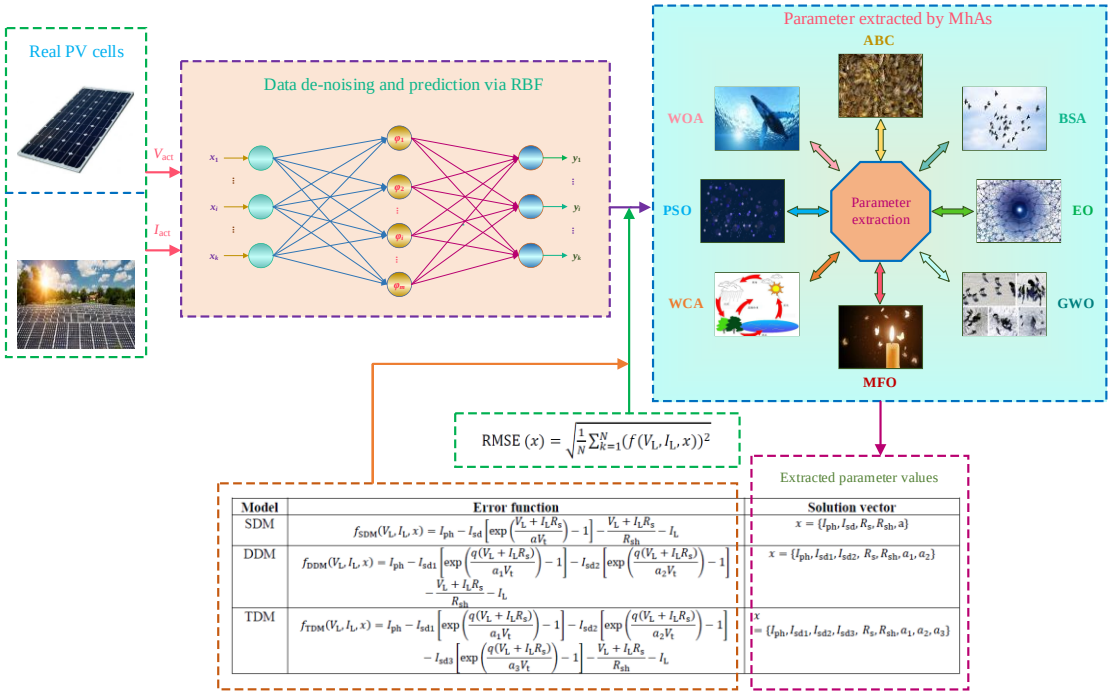

Figure 7. The topological structure of RBF.

The specific implementation process is as follows: collecting actual PV cell voltage and current data, then training RBF for data prediction and data de-noising to obtain de-noising current and de-noising current. In the end, using MhAs to optimize and iterate the data of cell models, SDM, DDM, and TDM, respectively, and finally obtain the optimal model parameters. Note that RMSE is used as the result evaluation standard in this article. The specific steps for executing RBF-MhAs are shown in Table 1.

Table 1. The identification steps of RBF-MhAs for PV parameter extraction.

1	Determine PV model;
2	Collect measured *I-V* data of PV;
3	Process measured *I-V* data by RBF;
4	Initialize population and parameters of various MhAs;
5	Set $t = 0$;
6	WHILE $t \leq t_{max}$
7	FOR1 $i = 1{:}n$
8	Compute the fitness value of the ith individual via Equation (5);
9	END FOR1
10	Adjust the roles of all individuals according to their fitness values;
11	FOR2 $i = 1{:}n$
12	Update solution of the ith individual based on its searching rule;
13	END FOR2
14	Set $t = t + 1$;
15	END WHILE
16	Output optimal parameters for PV.

4. Case Studies

In this section, RBF and eight typical MhAs were used to extract the parameters of three PV models, namely artificial bee colony (ABC) [33], bird swarm algorithm BSA [34], equilibrium optimizer (EO) [20], GWO [35], moth-fire algorithm (MFO) [36], particle swarm optimization (PSO) [37], water cycle algorithm (WCA) [38], and whale optimization algorithm (WOA) [39], and the reasons for choosing these eight algorithms are explained in Remark 1. Then, the actual operating conditions of the cell were set, especially low.

This article considered the extraction of parameters due to insufficient data and noise data extracted 26 pairs of data from R.T.C. France PV cell, based on the original 26 pairs of *I-V* data. RBF was used for preprocessing, de-noising, and data prediction, respectively. Lastly, 266 pairs of *I-V* data were ultimately predicted for parameter extraction research in multiple data. The specific data preprocessing results are shown in Figures 5 and 6.

Remark 1. *Based on a previous review article [11] on PV cell parameter identification, it is found that these eight MhAs have advantages such as simple models and fast identification speed in the field of parameter identification. Therefore, this study selected the above eight MhAs.*

The operating conditions of PV cells and the specific model parameter settings for various MhAs in this article are shown in Table 2. All studies were based on MATLAB 2022b and simulated using a personal computer with a performance of 3.0 GHz 12th Gen Intel (R) Core (TM) i5-12500 and 64 GB RAM.

Table 2. Model and algorithms parameter settings.

Types	Parameters	Value
PV	Irradiance	1000 W/m^2
	Temperature	33 °C
Algorithms	Maximum iterations	500
	Population size	30 (SDM) 50 (DDM) 70 (TDM)
	Run times	10

4.1. SDM Parameter Extraction

4.1.1. Noised Data

Table 3 summarizes the SDM parameter extraction results obtained through eight algorithms under different training data, where the symbol 'N' represents the results obtained using noised data and 'DN' represents the results obtained using de-noised data. From Table 3, it can be seen that after data de-noising, the RMSE obtained by the eight algorithms is smaller than that obtained by using noise data. In particular, the MFO algorithm has the largest decrease of 89.03%. The BSA algorithm has the smallest decrease, at 22.45%.

In addition, Figure 8 shows the RMSE convergence curves obtained by eight algorithms trained on two datasets. The results obtained based on data de-noising have smaller errors than those obtained from noise data.

Considering the impact of two different training data on the results, Figure 9 shows the boxplot of the RMSE distribution obtained by MhAs. It is obvious that after data noise reduction, the upper and lower bounds of the RMSE obtained by each algorithm or the RMSE median have decreased to a certain extent, and the RMSE outlier obtained by BSA, MFO, and WOA has disappeared. This sufficiently demonstrates that de-noising based on RBF data can significantly improve the accuracy and stability of MhAs in parameter extraction.

Table 3. Parameters identification results of noise data and de-noising data based on MhAs for SDM.

State	Algorithms	Data	Identified Parameters					RMSE
			I_{ph} (A)	I_{SD1} (A)	R_s (Ω)	R_{sh} (Ω)	a	
SDM	ABC	N	0.7658	1.0000×10^{-6}	0.0318	76.2020	1.6019	2.9400×10^{-2}
		DN	0.7610	9.9400×10^{-7}	0.0307	67.4567	1.6046	$\mathbf{3.3000 \times 10^{-3}}$
	BSA	N	0.7669	9.3400×10^{-7}	0.0318	60.5889	1.5939	2.9400×10^{-2}
		DN	0.7605	2.1100×10^{-7}	0.0385	54.6220	1.4397	$\mathbf{2.2800 \times 10^{-2}}$
	EO	N	0.7657	1.0000×10^{-6}	0.0314	99.9999	1.6015	2.9300×10^{-2}
		DN	0.7612	7.5500×10^{-7}	0.0320	60.3018	1.5726	$\mathbf{3.3000 \times 10^{-3}}$
	GWO	N	0.7670	6.5000×10^{-7}	0.0356	85.4718	1.5521	2.9700×10^{-2}
		DN	0.7647	3.9800×10^{-7}	0.0294	20.6894	1.5046	$\mathbf{6.9000 \times 10^{-3}}$
	MFO	N	0.7657	2.3800×10^{-7}	0.0378	48.7267	1.4482	3.0100×10^{-2}
		DN	0.7610	9.8400×10^{-7}	0.0307	71.3226	1.6032	$\mathbf{3.3000 \times 10^{-3}}$
	PSO	N	0.7651	6.4100×10^{-7}	0.0338	98.6639	1.5504	2.9500×10^{-2}
		DN	0.7610	1.0000×10^{-6}	0.0306	70.1421	1.6052	$\mathbf{3.3000 \times 10^{-3}}$
	WCA	N	0.7654	6.9700×10^{-7}	0.0333	93.8116	1.5598	2.9500×10^{-2}
		DN	0.7610	9.1100×10^{-7}	0.0311	68.7114	1.5941	$\mathbf{3.3000 \times 10^{-3}}$
	WOA	N	0.7662	5.9200×10^{-7}	0.0333	82.9164	1.5417	2.9600×10^{-2}
		DN	0.7593	3.0300×10^{-7}	0.0380	68.1910	1.4752	$\mathbf{4.3000 \times 10^{-3}}$

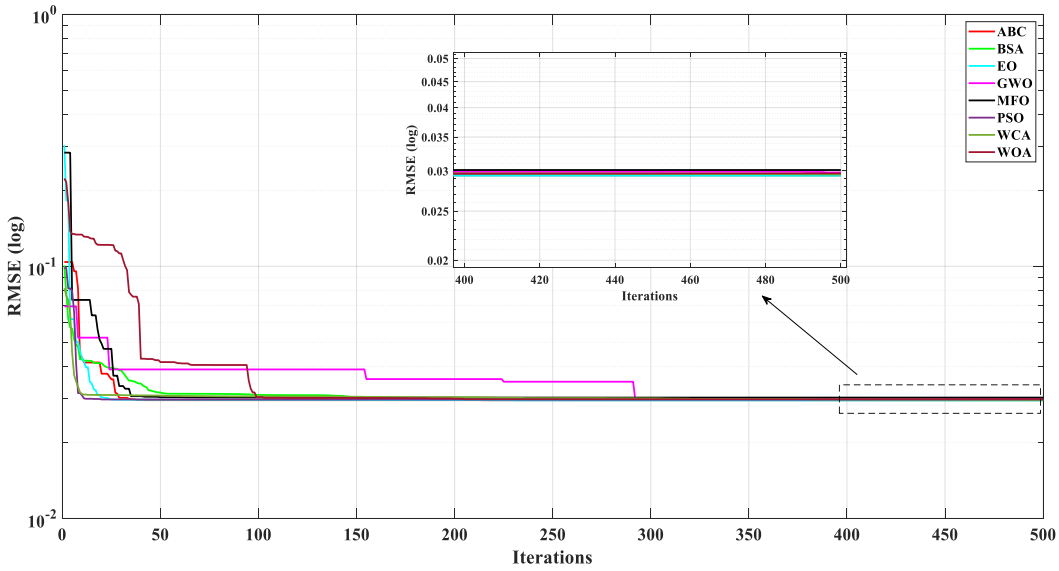

(**a**)

Figure 8. *Cont.*

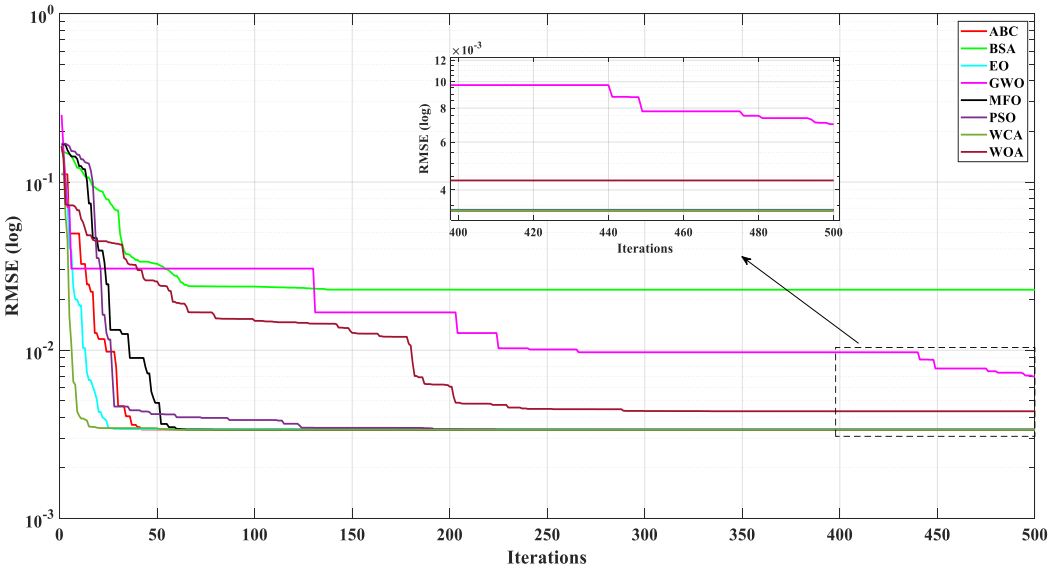

(**b**)

Figure 8. Convergence curves of RMSEs obtained by MhAs for SDM under noise data and de-noising data. (**a**) noise data and (**b**) de-noising data.

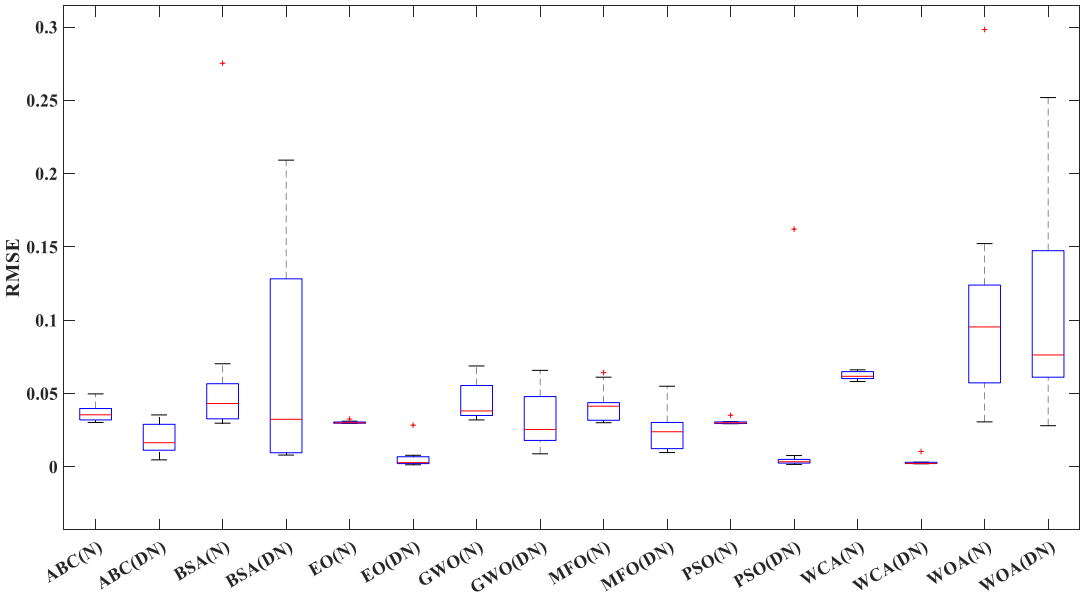

Figure 9. Boxplot of RMSEs obtained by MhAs for SDM under noise data and de-noising data.

Figure 10 shows the *I*-*V* and *P*-*V* characteristic curves obtained by SDM using MFO fitting among the eight algorithms under noise reduction data conditions. It can be seen that the fitted data is very close to the actual data, demonstrating excellent parameter identification accuracy. The correlation coefficient R_I^2 of *I*-*V* curve fitting is 99.57%, and the correlation coefficient R_P^2 of *P*-*V* curve fitting is 99.67%.

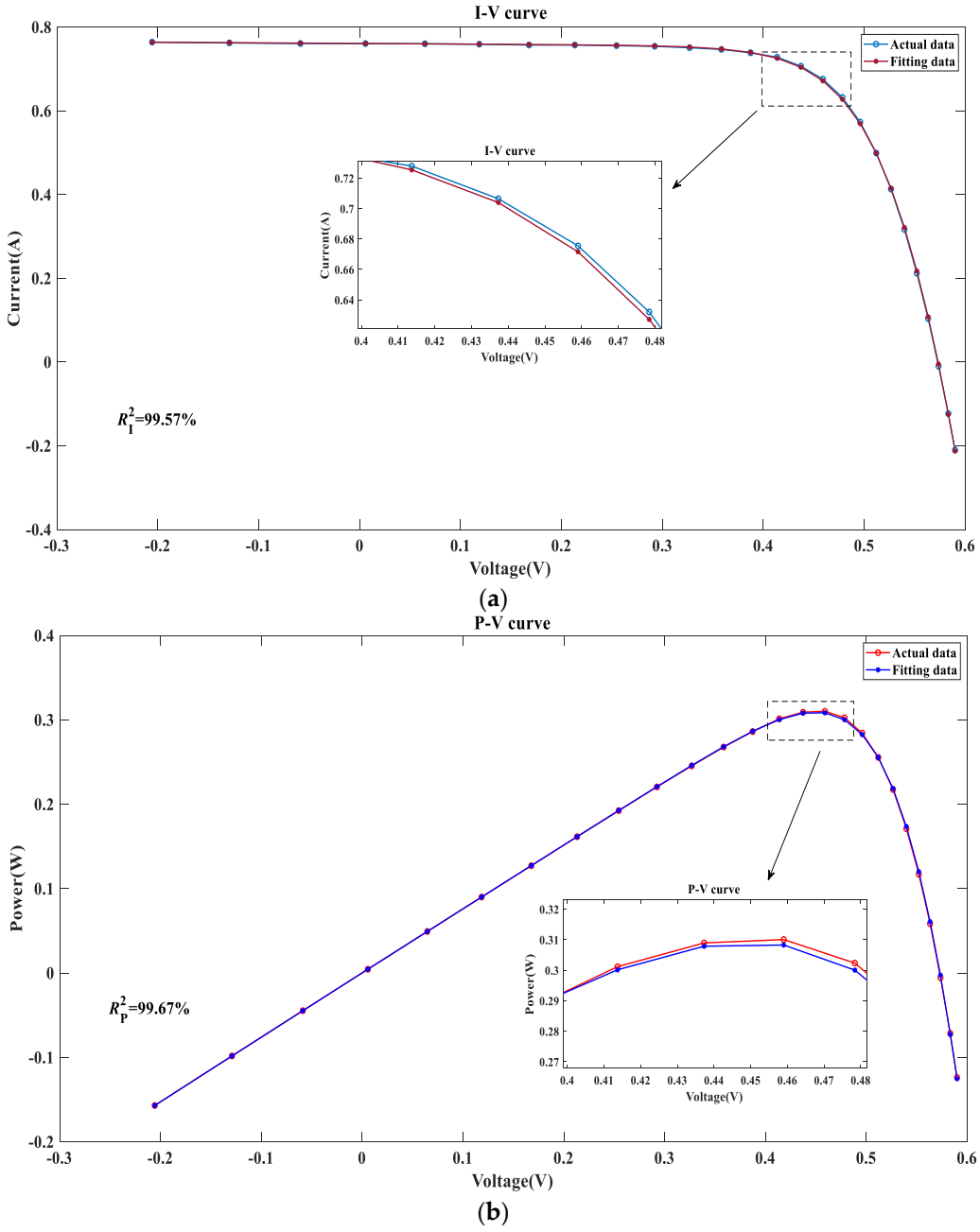

Figure 10. MFO for fitting curves based on de-noising data of SDM. (**a**) *I-V* curve and (**b**) *P-V* curve.

4.1.2. Insufficient Data

Table 4 summarizes the SDM parameter extraction results obtained by eight algorithms under both low and high data conditions, where the symbol 'O' represents the source data and 'P' represents the predicted data. It can be seen that, except for the WOA algorithm, which did not show a decrease in RMSE, the RMSE obtained by the other seven algorithms under the condition of predicted data is smaller than that obtained under the condition of source data. Among them, the BSA algorithm has the largest decrease, with 89.47%.

Table 4. Parameters identification results of original data and predicted data based on MhAs for SDM.

State	Algorithms	Data	Identified Parameters					RMSE
			I_{ph} (A)	I_{SD1} (A)	R_s (Ω)	R_{sh} (Ω)	a	
SDM	ABC	O	0.7610	9.9400×10^{-7}	0.0307	67.4567	1.6046	3.3000×10^{-3}
		P	0.7608	6.3000×10^{-7}	0.0329	70.6810	1.5517	$\mathbf{1.9000 \times 10^{-3}}$
	BSA	O	0.7605	2.1100×10^{-7}	0.0385	54.6220	1.4397	2.2800×10^{-2}
		P	0.7632	5.6900×10^{-7}	0.0330	42.5673	1.5410	$\mathbf{2.4000 \times 10^{-3}}$
	EO	O	0.7612	7.5500×10^{-7}	0.0320	60.3018	1.5726	3.3000×10^{-3}
		P	0.7604	7.7600×10^{-7}	0.0326	98.9046	1.5749	$\mathbf{1.9000 \times 10^{-3}}$
	GWO	O	0.7647	3.9800×10^{-7}	0.0294	20.6894	1.5046	6.9000×10^{-3}
		P	0.7601	3.7300×10^{-7}	0.0362	77.2725	1.4955	$\mathbf{1.3000 \times 10^{-3}}$
	MFO	O	0.7610	9.8400×10^{-7}	0.0307	71.3226	1.6032	3.3000×10^{-3}
		P	0.7605	8.6000×10^{-7}	0.0321	100.0000	1.5867	$\mathbf{2.1000 \times 10^{-3}}$
	PSO	O	0.7610	1.0000×10^{-6}	0.0306	70.1421	1.6052	3.3000×10^{-3}
		P	0.7609	4.7700×10^{-7}	0.0347	64.2417	1.5214	$\mathbf{1.2000 \times 10^{-3}}$
	WCA	O	0.7610	9.1100×10^{-7}	0.0311	68.7114	1.5941	3.0000×10^{-3}
		P	0.7608	1.0000×10^{-6}	0.0313	100.0000	1.6045	$\mathbf{2.4000 \times 10^{-3}}$
	WOA	O	0.7593	3.0300×10^{-7}	0.0380	68.1910	1.4752	4.3000×10^{-3}
		P	0.7516	8.1800×10^{-7}	0.0118	39.9892	1.5859	$\mathbf{3.0700 \times 10^{-2}}$

Figure 11 shows the RMSE convergence curves obtained by eight algorithms on two datasets, with smaller RMSE based on predicted data. However, due to the increase in training datasets, the convergence speed of each algorithm slows down.

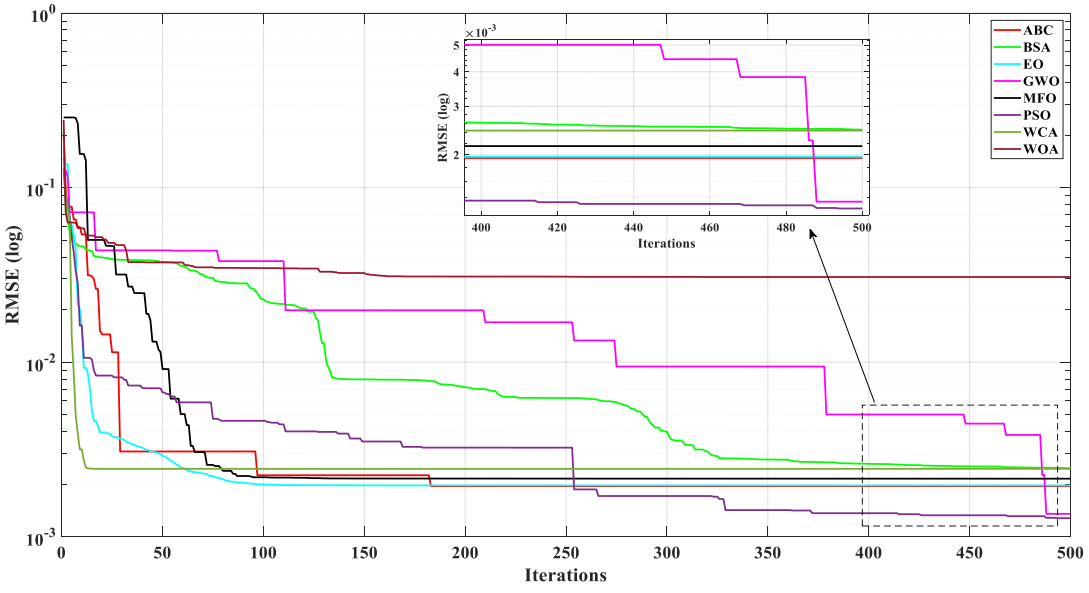

(**a**)

Figure 11. *Cont.*

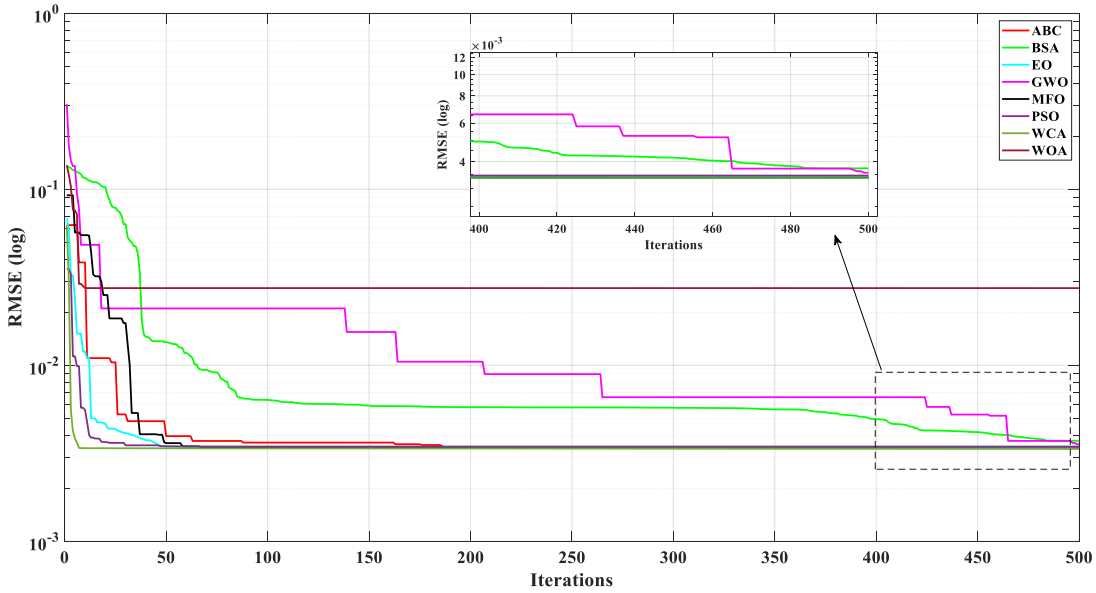

Figure 11. Convergence curves of RMSEs obtained by MhAs for SDM under original data and predicted data. (**a**) predicted data and (**b**) original data.

Figure 12 depicts the RMSE distribution boxplot obtained by eight algorithms. It can be seen that, except for the WCA algorithm, the upper and lower bounds of RMSE obtained based on predicted data have decreased.

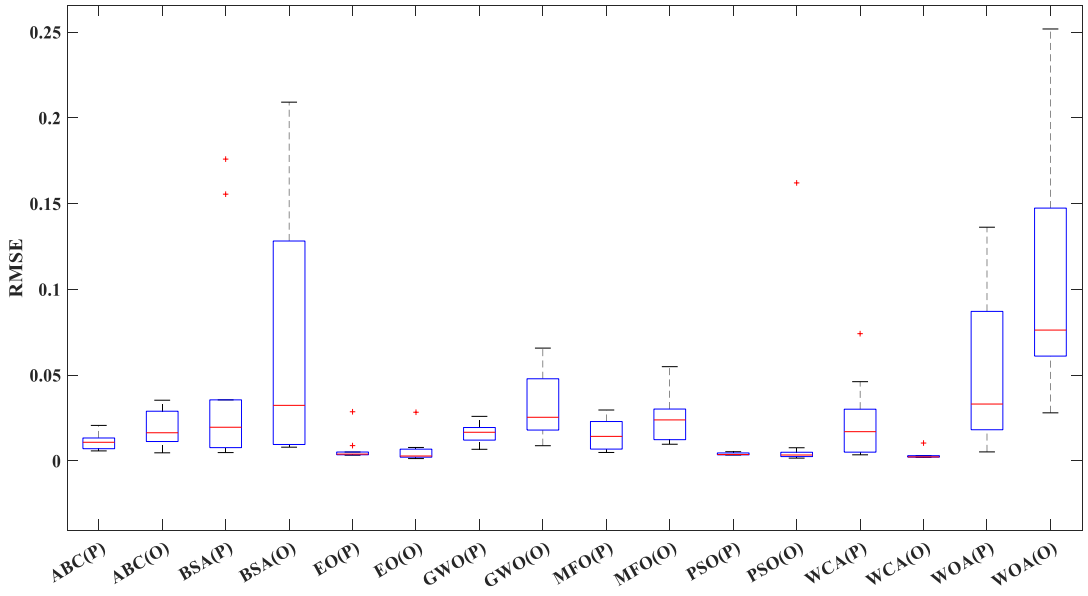

Figure 12. Boxplot of RMSEs obtained by MhAs for SDM under original data and predicted data.

4.2. DDM Parameter Extraction

4.2.1. Noised Data

Table 5 summarizes the parameter extraction results of the DDM model obtained by eight heuristic algorithms under the conditions of noise data and noise reduction data. It can be seen that the GWO algorithm obtained the highest RMSE amplitude, starting from 3.2100×10^{-2} decreases to 3.5000×10^{-3}, with a decrease of 89.10%. Under noise conditions, the DDM model has the smallest error obtained by MFO under eight heuristic algorithm optimizations, with an RMSE of 2.9100×10^{-2}. Under noise reduction

conditions, the MFO algorithm and WCA algorithm achieve the smallest error, with an RMSE of 3.3000×10^{-3}.

Table 5. Parameters identification results of noise data and de-noising data based on MhAs for DDM.

State	Algorithms	Data	Identified Parameters							RMSE
			I_{ph} (A)	I_{SD1} (A)	R_s (Ω)	R_{sh} (Ω)	a_1	I_{SD2} (A)	a_2	
DDM	ABC	N	0.7690	6.1500×10^{-7}	0.0287	73.9055	1.6797	9.7100×10^{-7}	1.6462	2.9200×10^{-2}
		DN	0.7617	6.4300×10^{-7}	0.0320	62.8954	1.9905	6.9700×10^{-7}	1.5689	$\mathbf{3.4000 \times 10^{-3}}$
	BSA	N	0.7666	7.5300×10^{-7}	0.0331	73.1427	1.8821	4.8300×10^{-7}	1.5312	2.9500×10^{-2}
		DN	0.7603	6.9600×10^{-7}	0.0289	99.6245	1.6456	4.2500×10^{-7}	1.5847	$\mathbf{3.7000 \times 10^{-3}}$
	EO	N	0.7682	8.1400×10^{-7}	0.0277	58.5882	1.6717	1.0000×10^{-6}	1.6794	2.9200×10^{-2}
		DN	0.7610	9.7600×10^{-7}	0.0288	80.6085	1.6365	3.5200×10^{-7}	1.6478	$\mathbf{3.4000 \times 10^{-3}}$
	GWO	N	0.7802	2.7100×10^{-7}	0.0361	11.3510	1.4721	4.5500×10^{-11}	1.0401	3.2100×10^{-2}
		DN	0.7616	2.3200×10^{-7}	0.0340	48.2361	1.8255	4.4700×10^{-7}	1.5202	$\mathbf{3.5000 \times 10^{-3}}$
	MFO	N	0.7670	1.0000×10^{-6}	0.0276	100.0000	1.7098	1.0000×10^{-6}	1.6699	2.9100×10^{-2}
		DN	0.7610	8.7400×10^{-7}	0.0308	72.0866	1.5919	3.3800×10^{-7}	2.0000	$\mathbf{3.3000 \times 10^{-3}}$
	PSO	N	0.7667	9.1900×10^{-7}	0.0298	100.0000	1.6107	1.0000×10^{-6}	1.8639	2.9200×10^{-2}
		DN	0.7607	2.6000×10^{-7}	0.0295	99.2881	1.6540	1.0000×10^{-6}	1.6278	$\mathbf{3.4000 \times 10^{-3}}$
	WCA	N	0.7664	1.0000×10^{-6}	0.0300	100.0000	1.6099	1.0000×10^{-6}	2.0000	2.9200×10^{-2}
		DN	0.7610	7.0700×10^{-7}	0.0310	69.2606	1.6205	2.4200×10^{-7}	1.5535	$\mathbf{3.3000 \times 10^{-3}}$
	WOA	N	0.7561	6.0700×10^{-7}	0.0094	28.1439	1.7688	6.6100×10^{-7}	1.5831	4.3000×10^{-2}
		DN	0.7599	2.5700×10^{-7}	0.0410	77.2374	1.5831	5.9800×10^{-8}	1.3593	$\mathbf{2.7400 \times 10^{-2}}$

Figure 13 shows the RMSE convergence curves obtained by eight algorithms under noise and de-noised data conditions. It can be seen that under the condition of de-noised data, the RMSE of parameter identification results has decreased to a certain extent.

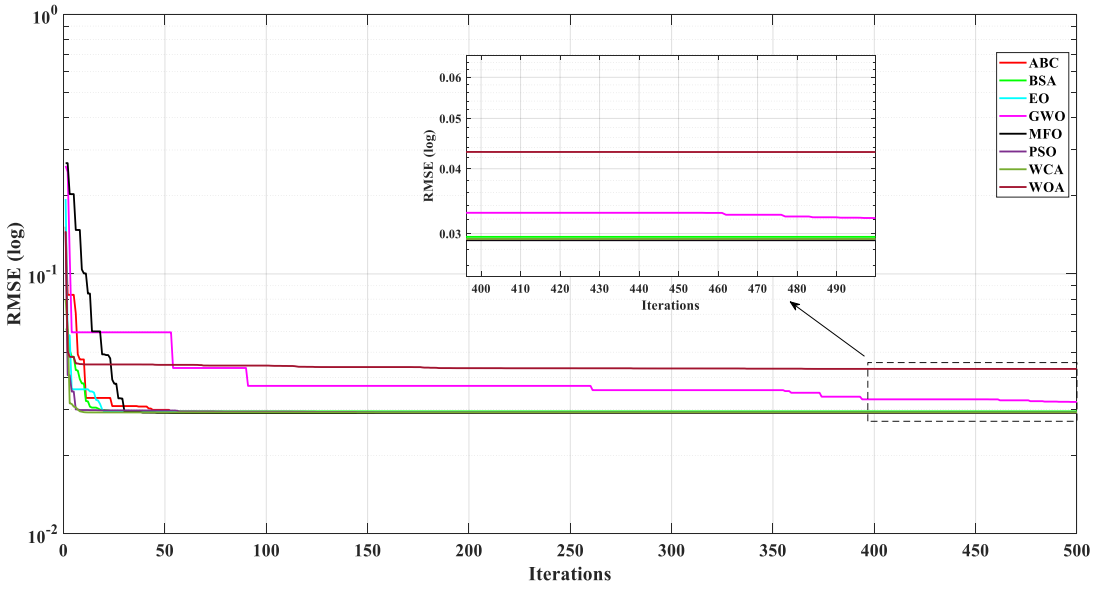

(**a**)

Figure 13. *Cont.*

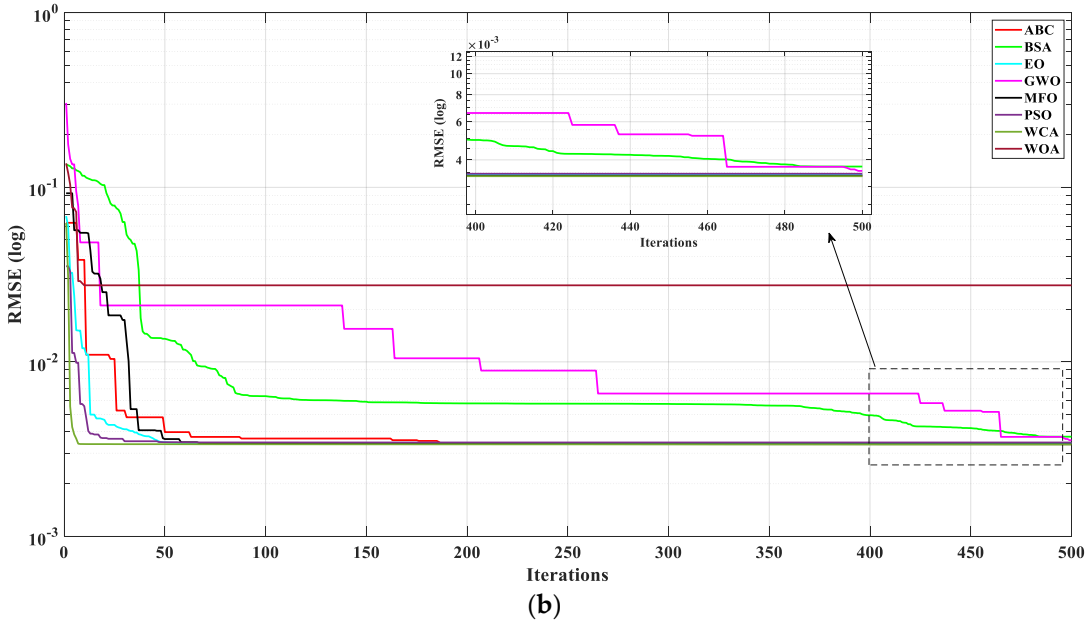

Figure 13. Convergence curves of RMSEs obtained by MhAs for DDM under noise data and de-noising data. (**a**) noise data and (**b**) de-noising data.

Figure 14 shows the RMSE distribution boxplot obtained by DDM under two data conditions. It can be seen that after data de-noising, the upper and lower bounds of the RMSE distribution of other algorithms except for WOA have decreased, and the median has also decreased to a certain extent.

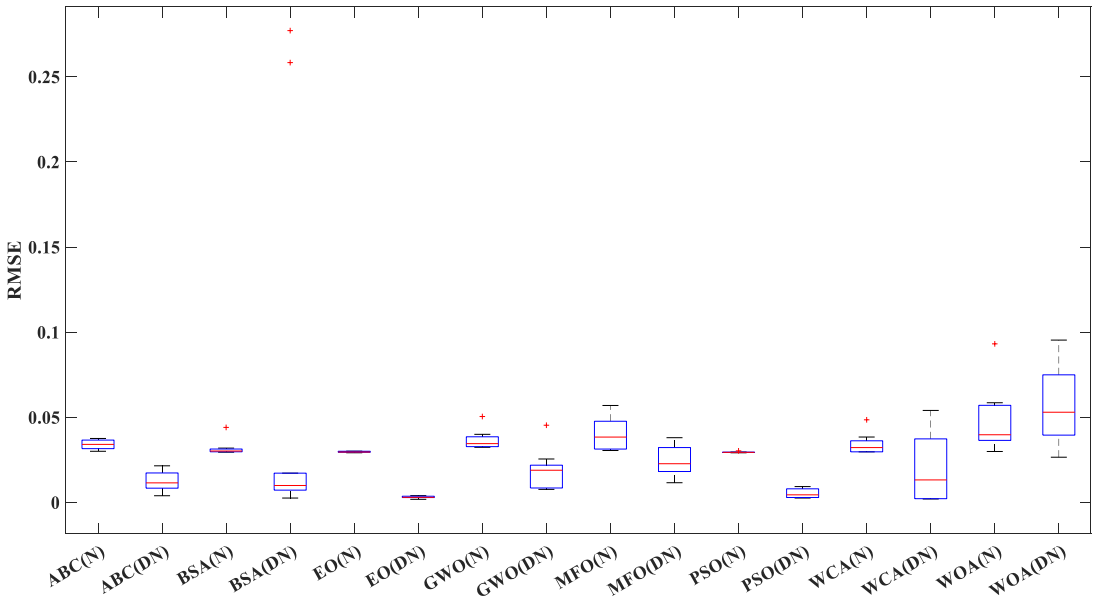

Figure 14. Boxplot of RMSEs obtained by MhAs for DDM under noise data and de-noising data.

Figure 15 shows the *I-V* curve and *P-V* curve obtained by DDM using the WCA algorithm under de-noised data conditions. WCA obtained the lowest RMSE and highest accuracy under de-noised data conditions. It can be seen from the figure that the fitting accuracy is very high. The correlation coefficient R_I^2 of *I-V* curve fitting is 99.57%, and the correlation coefficient R_P^2 of *P-V* curve fitting is 99.64%.

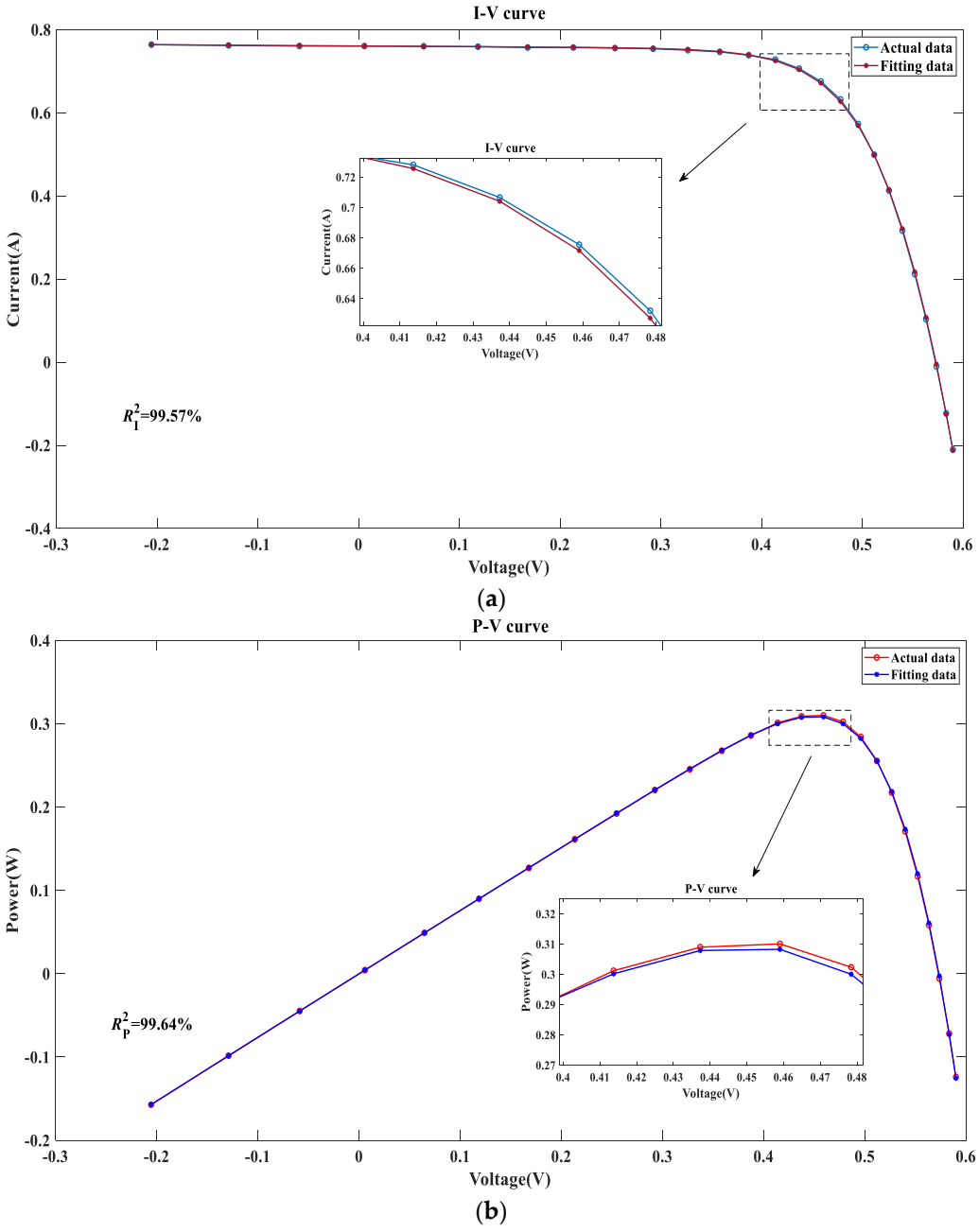

Figure 15. WCA for fitting curves based on de-noising data of DDM. (**a**) *I-V* curve and (**b**) *P-V* curve.

4.2.2. Insufficient Data

Table 6 shows the identification results of eight algorithms for the DDM model under both low and high data conditions. It can be seen that, except for the GWO algorithm, the RMSE obtained by other algorithms has decreased to a certain extent, and the accuracy is improving, especially low. The WCA algorithm has the largest downward decrease, at 72.73%.

Table 6. Parameters identification results of original data and predicted data based on MhAs for DDM.

State	Algorithms	Data	Identified Parameters							RMSE
			I_{ph} (A)	I_{SD1} (A)	R_s (Ω)	R_{sh} (Ω)	a_1	I_{SD2} (A)	a_2	
DDM	ABC	O	0.7617	6.4300×10^{-7}	0.0320	62.8954	1.9905	6.9700×10^{-7}	1.5689	3.4000×10^{-3}
		P	0.7613	6.8900×10^{-7}	0.0341	92.4257	2.0000	4.7400×10^{-7}	1.5256	$\mathbf{2.8000 \times 10^{-3}}$
	BSA	O	0.7603	6.9600×10^{-7}	0.0289	99.6245	1.6456	4.2500×10^{-7}	1.5847	3.7000×10^{-3}
		P	0.7619	5.3200×10^{-7}	0.0334	50.7943	1.5374	1.1900×10^{-7}	1.7620	$\mathbf{1.8000 \times 10^{-3}}$
	EO	O	0.7610	9.7600×10^{-7}	0.0288	80.6085	1.6365	3.5200×10^{-7}	1.6478	3.4000×10^{-3}
		P	0.7603	6.0400×10^{-11}	0.0329	99.4188	1.8292	7.2900×10^{-7}	1.5678	$\mathbf{1.8000 \times 10^{-3}}$
	GWO	O	0.7616	2.3200×10^{-7}	0.0340	48.2361	1.8255	4.4700×10^{-7}	1.5202	$\mathbf{3.5000 \times 10^{-3}}$
		P	0.7759	3.5500×10^{-7}	0.0253	10.7062	1.6016	5.0800×10^{-7}	1.5881	1.3500×10^{-2}
	MFO	O	0.7610	8.7400×10^{-7}	0.0308	72.0866	1.5919	3.3800×10^{-7}	2.0000	3.3000×10^{-3}
		P	0.7609	1.0000×10^{-6}	0.0311	100.0000	1.6059	1.6900×10^{-7}	2.0000	$\mathbf{2.5000 \times 10^{-3}}$
	PSO	O	0.7607	2.6000×10^{-7}	0.0295	99.2881	1.6540	1.0000×10^{-6}	1.6278	3.4000×10^{-3}
		P	0.7605	8.0200×10^{-7}	0.0344	80.5873	1.9185	3.5500×10^{-7}	1.4997	$\mathbf{1.4000 \times 10^{-3}}$
	WCA	O	0.7610	7.0700×10^{-7}	0.0310	69.2606	1.6205	2.4200×10^{-7}	1.5535	3.3000×10^{-3}
		P	0.7607	9.2800×10^{-7}	0.0369	56.0609	1.9618	1.8900×10^{-7}	1.4365	$\mathbf{9.0000 \times 10^{-4}}$
	WOA	O	0.7599	2.5700×10^{-7}	0.0410	77.2374	1.5831	5.9800×10^{-8}	1.3593	2.7400×10^{-2}
		P	0.7634	1.1900×10^{-7}	0.0426	37.9834	1.8100	1.8100×10^{-7}	1.4273	$\mathbf{8.8000 \times 10^{-3}}$

Figure 16 shows the iterative curves obtained under two data conditions of DDM. It is evident that the overall RMSE obtained under multiple data conditions is smaller than that obtained under insufficient data conditions, but the convergence speed under multiple data conditions is lower than that under insufficient data conditions.

Figure 17 shows the distribution of RMSE obtained by DDM under multiple and few data conditions. Except for the BSA algorithm, the difference between the upper and lower bounds of RMSE obtained by the other seven algorithms is smaller than that under insufficient data conditions. This fully demonstrates that after RBF data prediction, the stability of parameter identification results can be improved.

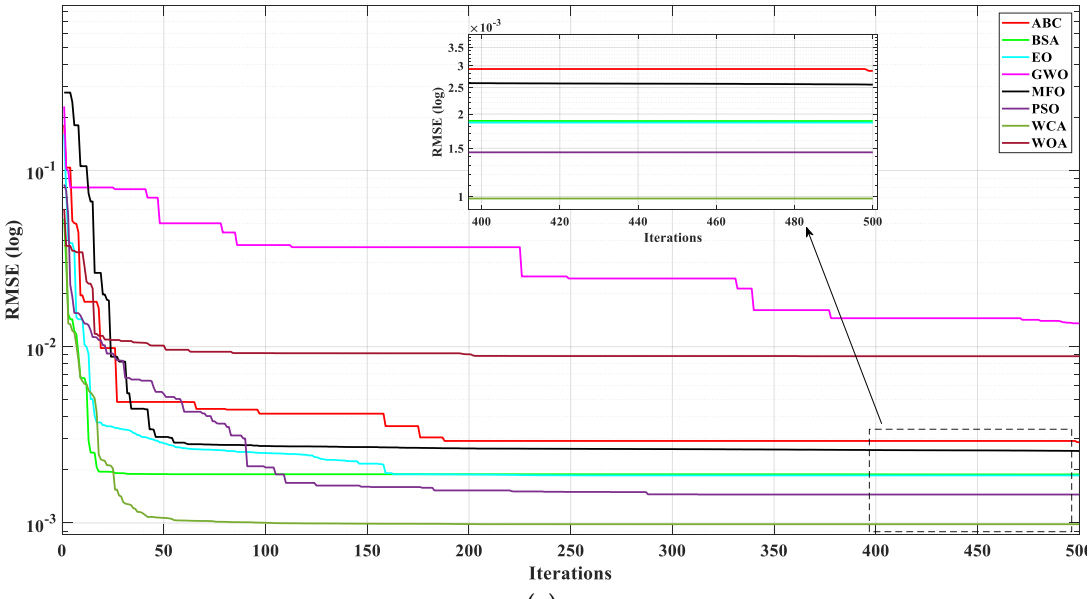

(**a**)

Figure 16. *Cont.*

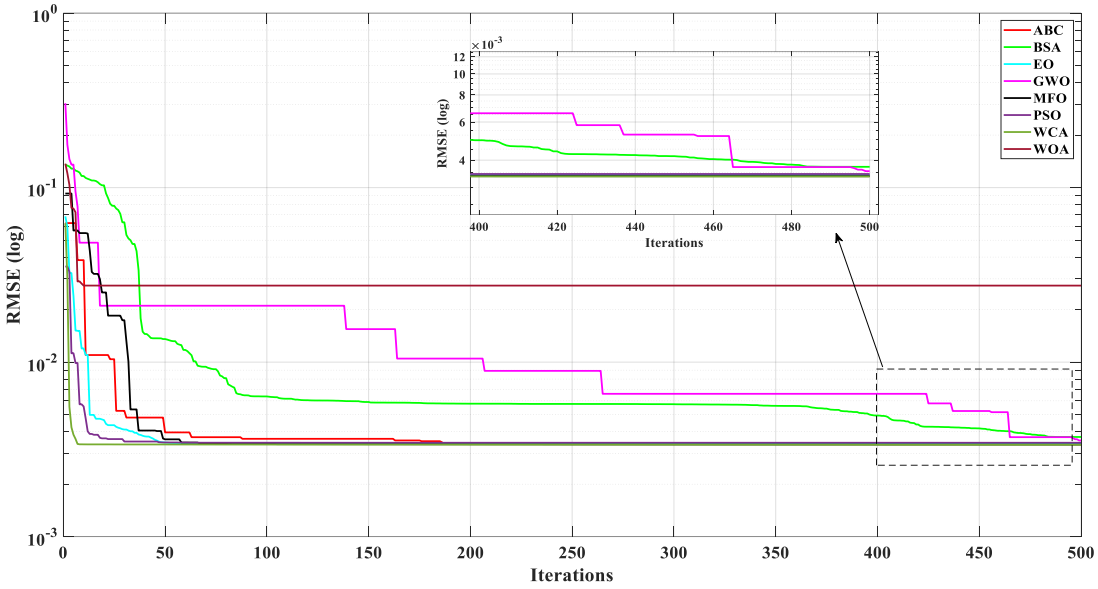

Figure 16. Convergence curves of RMSEs obtained by MhAs for DDM under predicted data and original data. (**a**) predicted data and (**b**) original data.

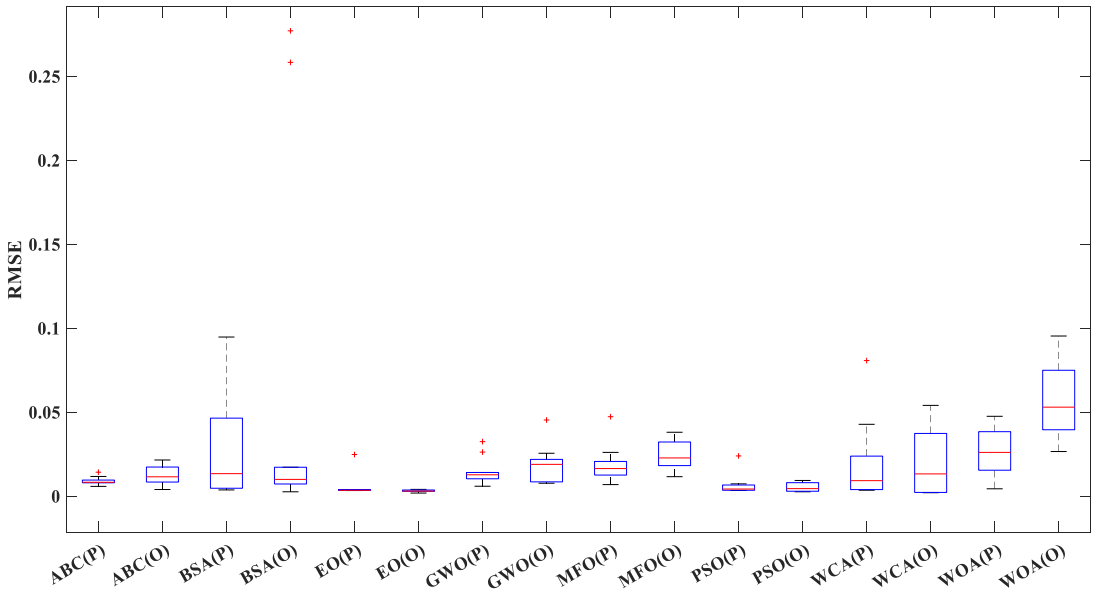

Figure 17. Boxplot of RMSEs obtained by MhAs for DDM under predicted data and original data.

4.3. TDM Parameter Extraction

4.3.1. Noised Data

Table 7 shows the results obtained by eight heuristic algorithms for TDM under noise and de-noising data conditions. It can be seen that after data de-noising, the RMSE of the parameter extraction results of all eight algorithms decreased, with the WOA algorithm having the largest decrease of 91.25%.

Figure 18 shows the RMSE iteration curves of the eight algorithms under the conditions of noised and de-noised data. It can be seen that the RMSE obtained by the eight algorithms has decreased.

Table 7. Parameters identification results of noise data and de-noising data based on MhAs for TDM.

State	Algorithms	Data	Identified Parameters									RMSE
			I_{ph} (A)	I_{SD1} (A)	R_s (Ω)	R_{sh} (Ω)	a_1	I_{SD2} (A)	a_2	I_{SD3} (A)	a_3	
TDM	ABC	N	0.7683	1.0000×10^{-6}	0.0249	67.7769	1.7591	9.2200×10^{-7}	1.8027	1.0000×10^{-6}	1.6893	2.9100×10^{-2}
		DN	0.7614	7.2100×10^{-7}	0.0299	87.3333	1.5962	3.3300×10^{-7}	1.7826	3.2000×10^{-7}	1.7098	$\mathbf{3.4000 \times 10^{-3}}$
	BSA	N	0.7659	7.6100×10^{-9}	0.0306	94.1495	1.9879	5.2900×10^{-7}	1.9502	1.0000×10^{-6}	1.6075	2.9300×10^{-2}
		DN	0.7647	1.4000×10^{-7}	0.0295	26.8613	1.9087	9.9700×10^{-7}	1.6086	2.5500×10^{-9}	1.8855	$\mathbf{5.3000 \times 10^{-3}}$
	EO	N	0.7670	1.0000×10^{-6}	0.0280	99.9999	1.9885	6.4500×10^{-7}	1.6576	8.2100×10^{-7}	1.6576	2.9100×10^{-2}
		DN	0.7611	5.3000×10^{-7}	0.0314	67.0230	1.6802	4.0500×10^{-7}	1.5436	1.8700×10^{-7}	1.9785	$\mathbf{3.3000 \times 10^{-3}}$
	GWO	N	0.7741	4.9200×10^{-7}	0.0304	20.3550	1.8385	6.4700×10^{-7}	1.5731	1.4000×10^{-8}	1.4351	3.0100×10^{-2}
		DN	0.7662	8.3600×10^{-7}	0.0267	20.5201	1.5988	3.7700×10^{-7}	1.7889	5.1600×10^{-8}	1.9444	$\mathbf{6.9000 \times 10^{-3}}$
	MFO	N	0.7676	1.0000×10^{-6}	0.0252	100.0000	1.7740	1.0000×10^{-6}	1.7323	9.6000×10^{-7}	1.7228	2.9000×10^{-2}
		DN	0.7610	1.0000×10^{-6}	0.0278	99.9996	1.9999	9.7400×10^{-7}	1.6195	1.0000×10^{-6}	2.0000	$\mathbf{3.3000 \times 10^{-3}}$
	PSO	N	0.7667	2.3200×10^{-7}	0.0299	90.7597	2.0000	1.0000×10^{-6}	1.6114	9.3500×10^{-7}	2.0000	2.9200×10^{-2}
		DN	0.7611	1.0000×10^{-6}	0.0277	100.0000	2.0000	1.0000×10^{-6}	1.6227	1.0000×10^{-6}	2.0000	$\mathbf{3.6000 \times 10^{-3}}$
	WCA	N	0.7677	1.0000×10^{-6}	0.0250	100.0000	1.7432	1.0000×10^{-6}	1.7432	1.0000×10^{-6}	1.7432	2.9000×10^{-2}
		DN	0.7610	9.0500×10^{-8}	0.0310	69.0199	1.5923	1.6900×10^{-7}	1.6066	6.6400×10^{-7}	1.5936	$\mathbf{3.3000 \times 10^{-3}}$
	WOA	N	0.7704	1.2000×10^{-6}	0.0326	28.5938	1.4334	4.9400×10^{-7}	1.5416	1.8500×10^{-7}	1.6259	2.9700×10^{-2}
		DN	0.7529	1.4900×10^{-8}	0.0073	45.6208	1.7808	4.7200×10^{-7}	1.6927	1.9500×10^{-7}	1.4585	$\mathbf{2.6000 \times 10^{-2}}$

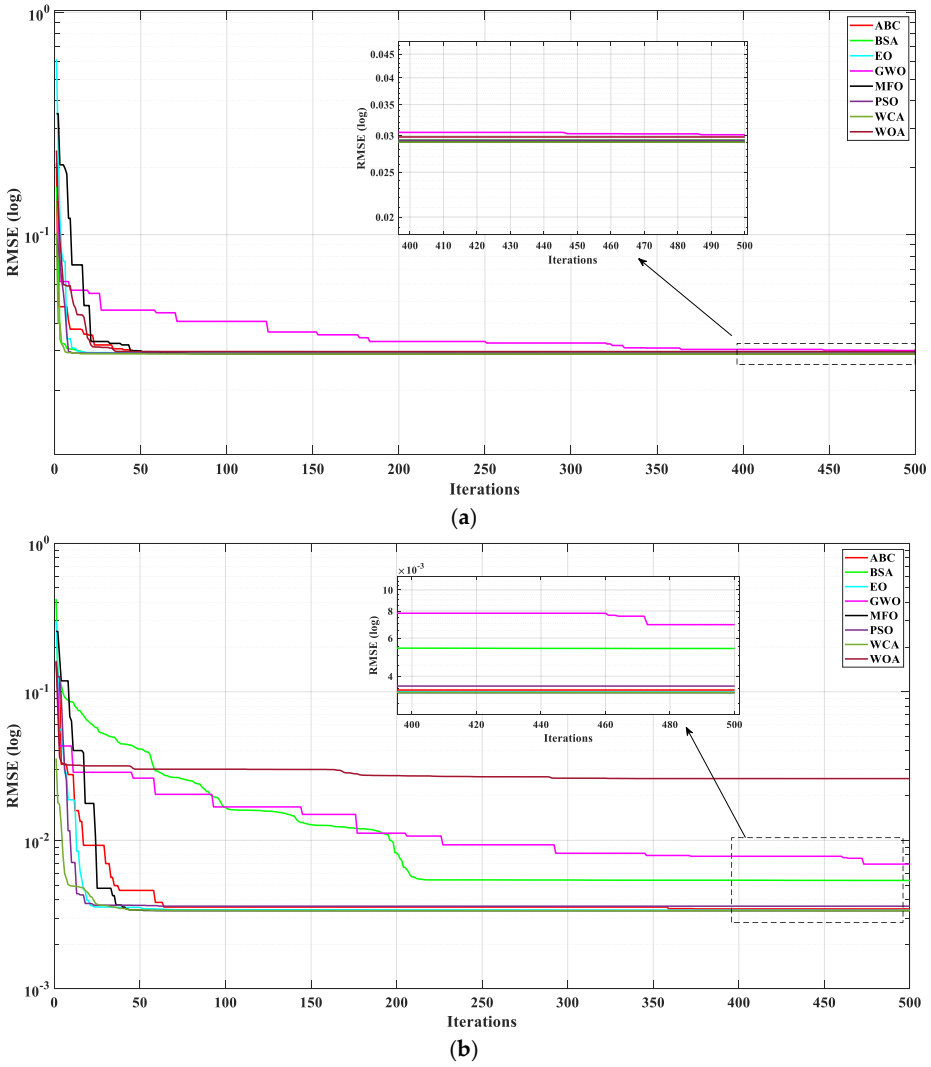

Figure 18. Convergence curves of RMSEs obtained by MhAs for TDM under noise data and de-noising data. (**a**) noise data and (**b**) de-noising data.

Figure 19 shows the boxplot of the RMSE distribution obtained by TDM under eight algorithms for parameter extraction. After data de-noising, the upper and lower bounds of RMSE in all eight algorithms showed a certain degree of decrease, and the RMSE values of abnormal results obtained by MFO and PSO algorithms were reduced. The accuracy and stability of parameter extraction were improved.

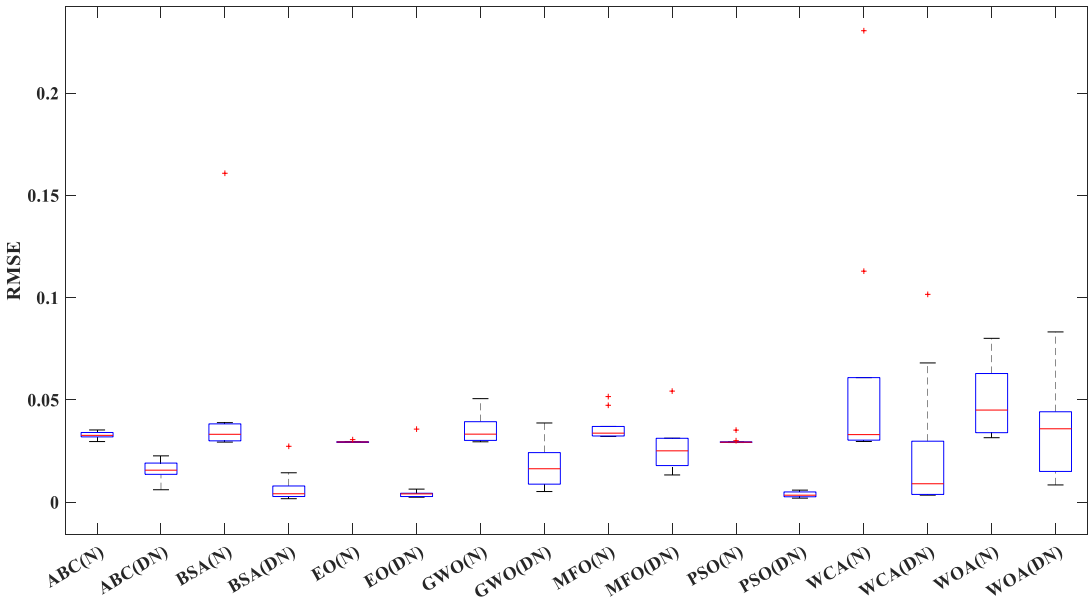

Figure 19. Boxplot of RMSEs obtained by MhAs for TDM under noise data and de-noising data.

Figure 20 shows the fitting curve obtained by WCA for TDM under noise reduction data conditions. Among the eight algorithms, WCA has the highest parameter identification accuracy, indicating very high fitting accuracy. The correlation coefficient R_I^2 of *I-V* curve fitting is 99.58%, and the correlation coefficient R_P^2 of *P-V* curve fitting is 99.65%.

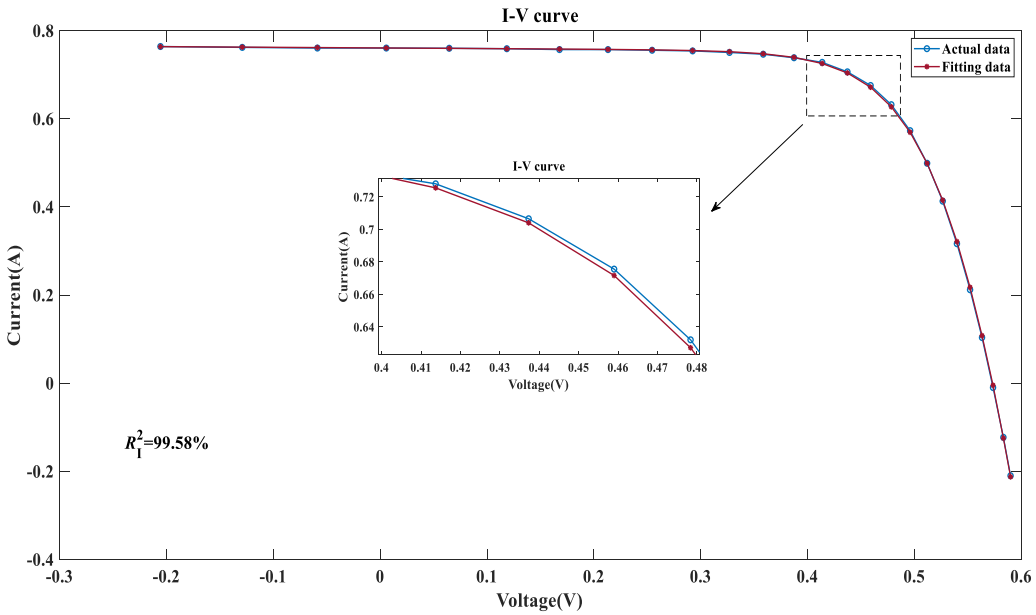

(**a**)

Figure 20. *Cont.*

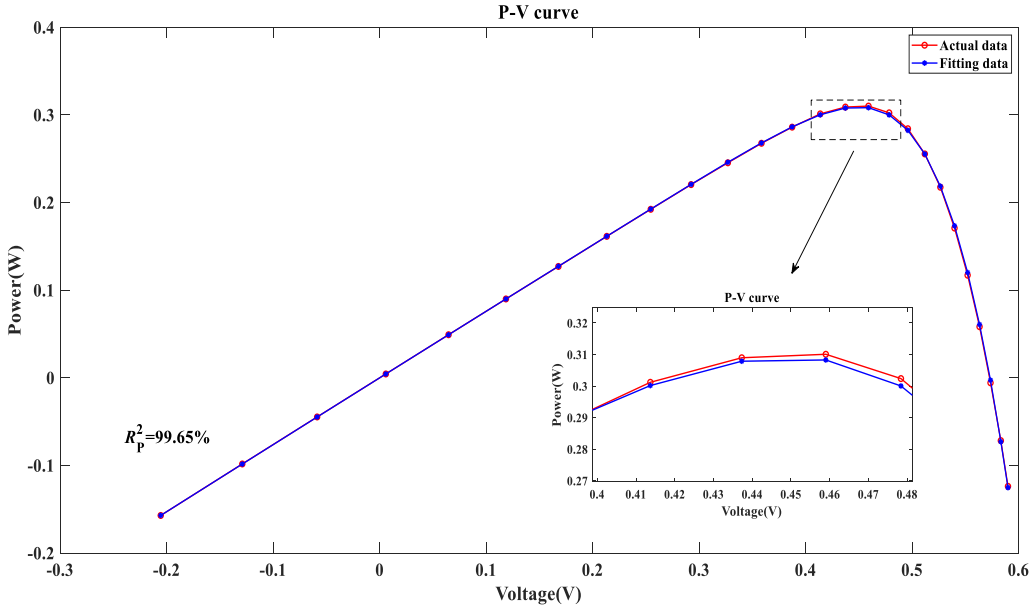

(**b**)

Figure 20. WCA for fitting curves based on de-noising data of TDM. (**a**) *I-V* curve and (**b**) *P-V* curve.

4.3.2. Insufficient Data

Table 8 shows the parameter extraction results of eight TDM algorithms under both low and high data conditions. All eight algorithms showed a decrease in RMSE, with the WOA algorithm having the largest decrease of 81.92%.

Table 8. Parameters identification results of original data and predicted data based on MhAs for TDM.

State	Algorithms	Data	Identified Parameters									RMSE
			I_{ph} (A)	I_{SD1} (A)	R_S (Ω)	R_{sh} (Ω)	a_1	I_{SD2} (A)	a_2	I_{SD3} (A)	a_3	
TDM	ABC	O	0.7614	7.2100×10^{-7}	0.0299	87.3333	1.5962	3.3300×10^{-7}	1.7826	3.2000×10^{-7}	1.7098	3.4000×10^{-3}
		P	0.7636	7.3500×10^{-7}	0.0345	48.5524	2.0000	3.3600×10^{-7}	1.4965	7.7900×10^{-7}	2.0000	$\mathbf{2.6000 \times 10^{-3}}$
	BSA	O	0.7647	1.4000×10^{-7}	0.0295	26.8613	1.9087	9.9700×10^{-7}	1.6086	2.5500×10^{-9}	1.8855	5.3000×10^{-3}
		P	0.7610	4.4300×10^{-8}	0.0334	70.2150	1.4577	3.7400×10^{-7}	1.5370	4.8700×10^{-7}	1.7586	$\mathbf{1.7000 \times 10^{-3}}$
	EO	O	0.7611	5.3000×10^{-7}	0.0314	67.0230	1.6802	4.0500×10^{-7}	1.5436	1.8700×10^{-7}	1.9785	3.3000×10^{-3}
		P	0.7596	5.7000×10^{-11}	0.0352	98.8942	1.8563	4.2400×10^{-7}	1.9774	3.9100×10^{-7}	1.5038	$\mathbf{1.4000 \times 10^{-3}}$
	GWO	O	0.7662	8.3600×10^{-7}	0.0267	20.5201	1.5988	3.7700×10^{-7}	1.7889	5.1600×10^{-8}	1.9444	6.9000×10^{-3}
		P	0.7559	9.6600×10^{-8}	0.0451	85.4750	1.9566	3.2000×10^{-8}	1.2794	1.2700×10^{-9}	1.7431	$\mathbf{5.8000 \times 10^{-3}}$
	MFO	O	0.7610	1.0000×10^{-6}	0.0278	99.9996	1.9999	9.7400×10^{-7}	1.6195	1.0000×10^{-6}	2.0000	3.3000×10^{-3}
		P	0.7606	4.6700×10^{-7}	0.0356	65.2163	2.0000	6.0000×10^{-8}	1.4026	3.5800×10^{-7}	1.5560	$\mathbf{2.4000 \times 10^{-3}}$
	PSO	O	0.7611	1.0000×10^{-6}	0.0277	100.0000	2.0000	1.0000×10^{-6}	1.6227	1.0000×10^{-6}	2.0000	3.6000×10^{-3}
		P	0.7612	6.2800×10^{-8}	0.0303	100.0000	2.0000	1.0000×10^{-6}	1.6110	7.0900×10^{-7}	2.0000	$\mathbf{2.9000 \times 10^{-3}}$
	WCA	O	0.7610	9.0500×10^{-8}	0.0310	69.0199	1.5923	1.6900×10^{-7}	1.6066	6.6400×10^{-7}	1.5936	3.3000×10^{-3}
		P	0.7607	1.2600×10^{-16}	0.0375	56.5387	1.0000	5.8700×10^{-10}	1.1327	4.5500×10^{-7}	1.5359	$\mathbf{2.4000 \times 10^{-3}}$
	WOA	O	0.7529	1.4900×10^{-8}	0.0073	45.6208	1.7808	4.7200×10^{-7}	1.6927	1.9500×10^{-7}	1.4585	2.6000×10^{-2}
		P	0.7657	9.9900×10^{-7}	0.0334	26.7065	1.9672	4.0300×10^{-7}	1.5327	2.9500×10^{-8}	1.4372	$\mathbf{4.7000 \times 10^{-3}}$

Figure 21 shows the RMSE iteration curves obtained by TDM under two different data conditions. It can be seen that after data prediction, the results obtained from parameter identification are more accurate. However, under insufficient data conditions, the convergence speed of the algorithm is faster.

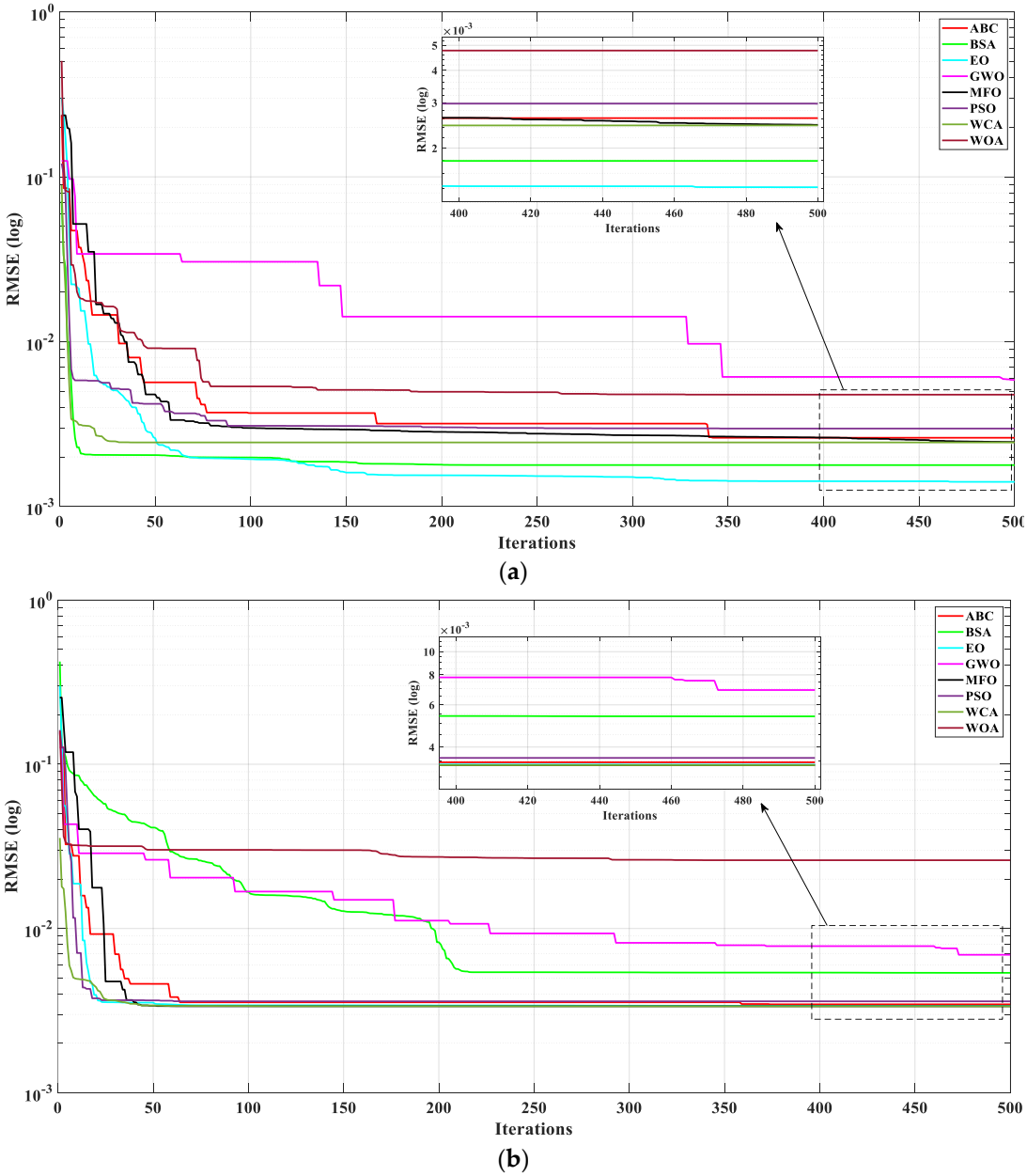

Figure 21. Convergence curves of RMSEs obtained by MhAs for TDM under predicted data and original data. (**a**) predicted data and (**b**) original data.

Figure 22 shows the distribution of TDM to RMSE under two data conditions. After data prediction, the algorithm identifies a smaller range of RMSE. Especially for WCA and WOA algorithms, the difference in RMSE between low and high data results is very significant, which fully demonstrates that data prediction can not only improve the accuracy of parameter identification but also improve the stability of identification algorithm performance.

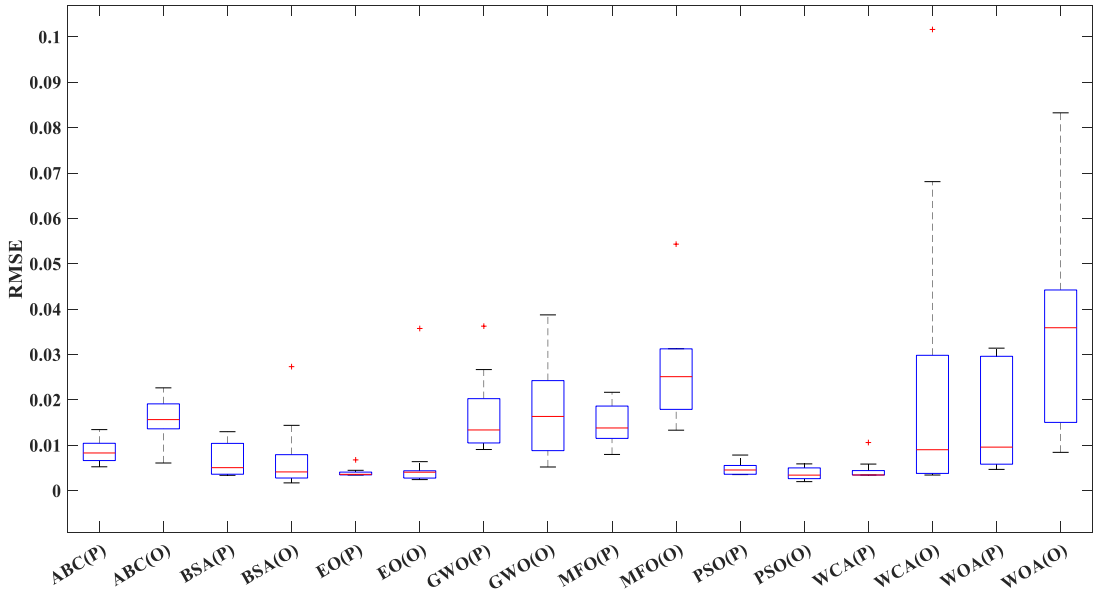

Figure 22. Boxplot of RMSEs obtained by MhAs for TDM under predicted data and original data.

5. Discussion

Table 9 is the summary of recent research in the field of PV cell parameter identification. Most studies did not consider the impact of both data volume and noise data on identification accuracy simultaneously. Compared to previous studies, the advantage of this article lies in considering both the insufficient measured *I-V* data and the impact of noise data and verifying three diode models [40,41]. Overall, due to the search randomness of MhAs, there are inevitable that a few RBF-MhAs were not ideal when extracting parameters from the three models of PV cell in this article. As shown in Table 3, using the WOA algorithm to extract parameters from SDM, the RMSE obtained based on predicted data conditions is greater than the RMSE obtained from insufficient data, resulting in abnormal situations.

Table 9. Summary of recent research on PV cell parameter identification.

Approach	Year	Cell Type	Data Process		Model Type			
			Data De-Noising	Data Prediction	No	SDM	DDM	TDM
WOA [14]	2020	KC200GT PV			√		√	
ELM-MhAs [12]	2021	R.T.C. France PV		√			√	
BP-IEO [20]	2021	R.T.C. France PV		√		√	√	√
APSO [15]	2022	MONO-SM110			√	√	√	√

In addition, by identifying the parameters of the three models, it can be distinctly seen that as the amount of data increases, the convergence speed of MhAs decreases, but the decrease is relatively small. However, after predicting and processing the data, the algorithm has improved to a certain extent in terms of parameter identification accuracy and stability. In addition, the study did not consider the effects of temperature and radiance on parameter identification accuracy. Future research should fully consider the impact of these environmental factors on PV cells.

6. Conclusions

This article uses a combination of RBF and MhAs to identify the parameters of PV cells, including SDM, DDM, and TDM. RBF is used to de-noise and predict the data and extract the parameters. The results are then compared with the original data extraction results. The

final results fully demonstrate that data processing can improve the accuracy and stability of parameter identification, especially with significant improvements. After data de-noising, TDM achieved an accuracy improvement of 91.25% compared to the source data, while SDM achieved an accuracy improvement of 89.03% after data de-noising. Compared with the previous research, the progressiveness of this paper is that the insufficient measured *I-V* data and the influence of noise data on the parameter identification accuracy are fully considered, and RBF and eight typical MhAs are used to identify the parameters of three diode models.

Therefore, in future research on PV cell parameter identification, analysis, and processing of measured current and voltage data can be carried out, which is conducive to improving the accuracy and stability of parameter identification. In addition, in practical applications, due to limited equipment and difficulty in obtaining measured data, using RBF for data prediction and parameter identification can solve the problem of data shortage to a certain extent and help reduce research costs.

Author Contributions: P.H.: writing the original draft and editing. X.X., S.L. and W.Q.: conceptualization. C.X. and B.Y.: visualization and contributed to the discussion of the topic. All authors have read and agreed to the published version of the manuscript.

Funding: This research received no external funding.

Conflicts of Interest: The authors declare that they have no known competing financial interests or personal relationships that could have appeared to influence the work reported in this paper.

References

1. Yang, B.; Liu, B.Q.; Zhou, H.Y.; Wang, J.B.; Yao, W.; Wu, S.C.; Shu, H.C.; Ren, Y.X. A Critical Survey of Technologies of Large Offshore Wind Farm Integration: Summarization, Advances, and Perspectives. *Prot. Control Mod. Power Syst.* **2022**, *7*, 17. [CrossRef]
2. Yang, B.; Li, Y.L.; Li, J.L.; Shu, H.C.; Zhao, X.Y.; Ren, Y.X.; Li, Q. Comprehensive Summarization of Solid Oxide Fuel Cell: Control: A State-of-the-art Review. *Prot. Control Mod. Power Syst.* **2022**, *7*, 36. [CrossRef]
3. Chen, Y.J.; Yang, B.; Guo, Z.X.; Wang, J.B.; Zhu, M.M.; Li, Z.L.; Li, Q.; Yu, T. Dynamic Reconfiguration for TEG Systems under Heterogeneous Temperature Distribution via Adaptive Coordinated Seeker. *Prot. Control Mod. Power Syst.* **2022**, *7*, 38. [CrossRef]
4. Yang, B.; Wang, J.B.; Zhang, M.T.; Shu, H.C.; Yu, T.; Zhang, X.S.; Yao, W.; Sun, L.M. A State-of-The-Art Survey of Solid Oxide Fuel Cell Parameter Identification: Modelling, Methodology, and Perspectives. *Energy Convers. Manag.* **2020**, *213*, 112856. [CrossRef]
5. Guo, L.; Chen, W.R.; Jia, J.B.; Han, M.; Liu, Y.H. BP Neural Network Modeling of Photovoltaic Cells based on Particle Swarm Optimization Algorithm. *Adv. Technol. Electr. Eng. Energy* **2011**, *30*, 84–88.
6. Ma, S.Q. Research on Model and V-I Characteristic of Photovoltaic Cell. *Power Technol.* **2013**, *137*, 1396–1405.
7. You, H.X. Analysis of Factors Influencing the Efficiency of Photovoltaic Power Generation. *Energy Technol. Manag.* **2022**, *47*, 147–149.
8. Diao, M.J. Modeling of Photovoltaic Cells and MPPT Simulation Analysis. *Telecom Power Technol.* **2018**, *35*, 30–32.
9. Zhang, C.J.; Zhao, Z.G.; Sang, H.T. Review of Photovoltaic Cells Modelling. *Power Technol.* **2016**, *40*, 927–930.
10. Shi, N.; Zhou, S.Q.; Li, Y.Z.; Zhu, X.H. PV Cell Modeling Based on Bezier Function. *Power Syst. Technol.* **2015**, *39*, 2195–2200.
11. Yang, B.; Wang, J.B.; Zhang, X.S.; Yu, T.; Yao, W.; Shu, H.C.; Zeng, F.; Sun, L.M. Comprehensive Overview of Meta-heuristic Algorithm Applications on PV Cell Parameter Identification. *Energy Convers. Manag.* **2020**, *208*, 112595. [CrossRef]
12. Liu, B.; Tan, Z.K.; Tang, S.Q.; Lin, C.H.; Gao, J.P. Photovoltaic Cell Parameter Extraction using Data Prediction based on A Meta-heuristic Algorithm. *Power Syst. Prot. Control* **2021**, *49*, 72–79.
13. Li, G.C. Parameter Identification and Simulation of Photovoltaic Cell Modules based on Improved Cuckoo Search. *J. Jiamusi Univ.* **2015**, *33*, 88–92.
14. Shi, J.F.; Lei, H.; Shi, C. Parameter Identification of Photovoltaic System based on Whale Optimization Algorithm. *Inf. Technol.* **2020**, *10*, 160–165.
15. Zhu, X.H.; Zhong, J.W.; Shi, N.; Fu, Z.; Liu, Z.W. Parameter Identification of Photovoltaic Cells based on Improved Adaptive Particle Swarm Optimization Algorithm. *J. Heilongjiang Univ. Sci. Technol.* **2022**, *6*, 786–789.
16. Nayak, B.; Mohapatra, A.; Mohanty, K.B. Parameter Estimation of Single Diode PV Module based on GWO Algorithm. *Renew. Energy* **2019**, *30*, 1–12.
17. Fathy, A.; Rezk, H. Parameter Estimation of Photovoltaic System using Imperialist Competitive Algorithm. *Renew. Energy* **2017**, *17*, 307–320. [CrossRef]
18. Yu, K.J.; Qu, B.Y.; Yue, C.T.; Ge, S.L.; Xu, C.; Jing, L. A Performance-guided JAYA Algorithm for Parameters Identification of Photovoltaic Cell and Module. *Appl. Energy* **2019**, *237*, 241–257. [CrossRef]

19. Qais, M.H.; Hasanien, H.M.; Alghuwainem, S.; Nouh, A.S. Coyote Optimization Algorithm for Parameters Extraction of Three-diode Photovoltaic Models of Photovoltaic Modules. *Energy* **2019**, *187*, 116001. [CrossRef]
20. Wang, J.B.; Yang, B.; Li, D.Y.; Zeng, C.Y.; Chen, Y.J.; Guo, Z.X.; Zhang, X.S.; Tan, T.; Shu, H.C.; Yu, T. Photovoltaic Cell Parameter Estimation based on Improved Equilibrium Optimizer Algorithm. *Energy Convers. Manag.* **2021**, *236*, 114051. [CrossRef]
21. Chen, X.; Ding, K.; Zhang, J.W.; Yang, Z.N.; Liu, Y.J.; Yang, H. A Two-stage Method for Model Parameter Identification based on the Maximum Power Matching and Improved Flow Direction Algorithm. *Energy Convers. Manag.* **2023**, *278*, 116712. [CrossRef]
22. Muneeswaran, V.; Rajasekaran, D.M.P. Performance Evaluation of Radial Basis Function Networks Based on Tree Seed Algorithm. In Proceedings of the 2016 International Conference on Circuit, Power and Computing Technologies, Nagercoil, India, 18–19 March 2016; pp. 1–4.
23. Yang, B.; Guo, Z.X.; Yang, Y.; Chen, Y.J.; Zhang, R.; Su, K.Y.; Sun, H.C.; Yu, T.; Zhang, X.S. Extreme Learning Machine based Meta-heuristic Algorithms for Parameter Extraction of Solid Oxide Fuel Cells. *Appl. Energy* **2021**, *303*, 117630. [CrossRef]
24. Long, W.; Wu, T.B.; Xu, M.; Tang, M.Z.; Cai, S.H. Parameters Identification of Photovoltaic Models by Using an Enhanced Adaptive Butterfly Optimization Algorithm. *Energy* **2021**, *229*, 120750. [CrossRef]
25. Zhang, T.T.; Jiang, H.H.; Yue, W.; Si, C.; Yuan, M. Adaptive Control Based on RBF Neural Network for Electro-optical System. *Acta Armamentarii* **2022**, *43*, 556–564.
26. Zhao, Z.R.; Pan, P.C.; Wu, T. Photovoltaic MPPT Method Based on APID-RBF Neural Network. *Proc. CSU-EPSA* **2023**, *15*, 1–9.
27. Andersen, H.C.; Lorfi, A.; Westphal, L.C. Comments on Functional Equivalence Between Radial Basis Function Networks and Fuzzy Inference Systems. *IEEE Trans. Neural Netw.* **1998**, *9*, 1529–1531. [CrossRef] [PubMed]
28. Chen, Q.; Zhang, S.X.; Cheng, H.Z.; Wang, S.P.; Yuan, K.; Song, Y.; Han, F. Probabilistic Energy Flow Calculation for Integrated Energy Systems Based on Radial Basis Function-stochastic Response Surface Method. *Proc. CSEE* **2022**, *42*, 8075–8088.
29. Liu, G.; Gao, C.L.; Hu, W.J.; Zhu, Z.C.; Liu, Y.P. Optimization Design of Transformer Electrostatic Ring Structure based on ESLE Sampling and Radial Basis Function Response Surface Method. *Trans. China Electrotech. Soc.* **2023**, *38*, 1–14.
30. Amir, N.; Mohammad, H.S.; Mohsen, Y. Developing and Multi-Objective Optimization of a Combined Energy Absorber Structure Using Polynomial Neural Networks and Evolutionary Algorithms. *Lat. Am. J. Solids Struct.* **2016**, *13*, 2552–2572.
31. Amir, N.; Payman, G.; Jahangir, T. On the Crashworthiness Optimisation of a New Multi-corner Tube under Axial Loading. *Ships Offshore Struct.* **2022**. [CrossRef]
32. Khadivi, P.; Tandon, R.; Ramakrishnan, N. Online Denoising of Discrete Noisy Data. In Proceedings of the 2015 IEEE International Symposium on Information Theory, Hong Kong, China, 14–19 June 2015; pp. 671–675.
33. Oliva, D.; Cuevas, E.; Pajares, G. Parameter Identification of Solar Cells Using Artificial Bee Colony Optimization. *Energy* **2014**, *72*, 93–102. [CrossRef]
34. Zhang, J.N.; Xia, K.; He, Z.P.; Fan, S.R. Dynamic Multi-swarm Differential Learning Quantum Bird Swarm Algorithm and Its Application in Random Forest Classification Model. *Comput. Intell. Neurosci.* **2020**, *1*, 6858541. [CrossRef] [PubMed]
35. Yang, B.; Wang, J.B.; Yu, L.; Shu, H.C.; Yu, T.; Zhang, X.S.; Yao, W.; Sun, L.M. A Critical Survey on Proton Exchange Membrane Fuel Cell Parameter Estimation using Meta-Heuristic Algorithms. *J. Clean. Prod.* **2020**, *265*, 121660. [CrossRef]
36. Zhang, H.L.; Heidari, A.A.; Wang, M.J.; Zhang, L.J.; Chen, H.L.; Li, C.Y. Orthogonal Nelder-mead Moth Flame Method for Parameters Identification of Photovoltaic Modules. *Energy Convers. Manag.* **2020**, *211*, 112764. [CrossRef]
37. Ye, M.Y.; Wang, X.D.; Xu, Y.S. Parameter Extraction of Solar Cells using Particle Swarm Optimization. *J. Appl. Phys.* **2009**, *105*, 094502. [CrossRef]
38. Sadollah, A.; Eskandar, H.; Bahreininejad, A.; Kim, J.H. Water Cycle Algorithm with Evaporation Rate for Solving Constrained and Unconstrained Optimization Problems. *Appl. Soft Comput. J.* **2015**, *30*, 58–71. [CrossRef]
39. Kumar, C.H.S.; Rao, R.S. A Novel Global MPP Tracking of Photovoltaic System based on Whale Optimization Algorithm. *Int. J. Renew. Energy Dev.* **2016**, *5*, 225–232. [CrossRef]
40. Saibal, M.; Ashok, K.A.; Deepak, K.S. Novel Lyapunov-based Rapid and Ripple-Free MPPT Using a Robust Model Reference Adaptive Controller for Solar PV System. *Prot. Control Mod. Power Syst.* **2023**, *8*, 13.
41. Sheetal, S.; Sanju, S.; Gupta, S.K.; Rajeev, K. Solar-PV Inverter for the Overall Stability of Power Systems with Intelligent MPPT Control of DC-Link Capacitor Voltage. *Prot. Control Mod. Power Syst.* **2023**, *8*, 15.